CrossMark

The ALMA-QUARKS Survey. I. Survey Description and Data Reduction

Xunchuan Liu (刘训川)[1] , Tie Liu[1], Lei Zhu[2], Guido Garay[3], Hong-Li Liu[4], Paul Goldsmith[5], Neal Evans[6], Kee-Tae Kim[7,22],
Sheng-Yuan Liu[8], Fengwei Xu[9,10], Xing Lu[1], Anandmayee Tej[11] , Xiaofeng Mai[1], Leonardo Bronfman[3], Shanghuo Li[12],
Diego Mardones[3], Amelia Stutz[13], Ken'ichi Tatematsu[14] , Ke Wang[9], Qizhou Zhang[15] , Sheng-Li Qin[4], Jianwen Zhou[16],
Qiuyi Luo[1,17], Siju Zhang[9], Yu Cheng[18], Jinhua He[19,2,3], Qilao Gu[1] , Ziyang Li[1,4], Zhenying Zhang[1,4], Suinan Zhang[1],
Anindya Saha[11] , Lokesh Dewangan[20], Patricio Sanhueza[18,21], and Zhiqiang Shen[1]

[1] Shanghai Astronomical Observatory, Chinese Academy of Sciences, Shanghai 200030, China; liuxunchuan@shao.ac.cn, liutie@shao.ac.cn
[2] Chinese Academy of Sciences South America Center for Astronomy, National Astronomical Observatories, Chinese Academy of Sciences, Beijing 100101, China
lzhupku@gmail.com
[3] Departamento de Astronomía, Universidad de Chile, Las Condes, 7591245 Santiago, Chile; guido@das.uchile.cl
[4] School of Physics and Astronomy, Yunnan University, Kunming 650091, China; hongliliu2012@gmail.com
[5] Jet Propulsion Laboratory, California Institute of Technology, 4800 Oak Grove Drive, Pasadena CA 91109, USA
[6] Department of Astronomy, The University of Texas at Austin, TX 78712-1205, USA
[7] Korea Astronomy and Space Science Institute, 776 Daedeokdae-ro, Yuseong-gu, Daejeon 34055, Republic of Korea
[8] Institute of Astronomy and Astrophysics, Academia Sinica, Roosevelt Road, Taipei 10617, China
[9] Kavli Institute for Astronomy and Astrophysics, Peking University, Beijing 100871, China
[10] Department of Astronomy, School of Physics, Peking University, Beijing 100871, China
[11] Indian Institute of Space Science and Technology, Thiruvananthapuram 695 547, Kerala, India
[12] Max Planck Institute for Astronomy, Königstuhl 17, D-69117 Heidelberg, Germany
[13] Departamento de Astronomía, Universidad de Concepción, Casilla 160-C, Concepción, Chile
[14] Nobeyama Radio Observatory, National Astronomical Observatory of Japan, National Institutes of Natural Sciences, 462-2 Nobeyama, Minamimaki, Minamisaku,
Nagano 384-1305, Japan
[15] Center for Astrophysics | Harvard & Smithsonian, 60 Garden Street, Cambridge, MA 02138, USA
[16] Max-Planck-Institut für Radioastronomie, Auf dem Hügel 69, D-53125 Bonn, Germany
[17] School of Astronomy and Space Sciences, University of Chinese Academy of Sciences, Beijing 100049, China
[18] National Astronomical Observatory of Japan, 2-21-1 Osawa, Mitaka, Tokyo, 181-8588, Japan
[19] Yunnan Observatories, Chinese Academy of Sciences, Kunming 650216, China
[20] Physical Research Laboratory, Navrangpura, Ahmedabad-380 009, India
[21] Astronomical Science Program, The Graduate University for Advanced Studies, SOKENDAI, 2-21-1 Osawa, Mitaka, Tokyo 181-8588, Japan
[22] University of Science and Technology, Korea (UST), 217 Gajeong-ro, Yuseong-gu, Daejeon 34113, Republic of Korea

Abstract

This paper presents an overview of the QUARKS survey, which stands for "Querying Underlying mechanisms of massive star formation with ALMA-Resolved gas Kinematics and Structures." The QUARKS survey is observing 139 massive clumps covered by 156 pointings at Atacama Large Millimeter/submillimeter Array (ALMA) Band 6 ($\lambda \sim 1.3$ mm). In conjunction with data obtained from the ALMA-ATOMS survey at Band 3 ($\lambda \sim 3$ mm), QUARKS aims to carry out an unbiased statistical investigation of massive star formation process within protoclusters down to a scale of 1000 au. This overview paper describes the observations and data reduction of the QUARKS survey, and gives a first look at an exemplar source, the mini-starburst Sgr B2(M). The wide-bandwidth (7.5 GHz) and high-angular-resolution ($\sim 0\rlap{.}''3$) observations of the QUARKS survey allow for the resolution of much more compact cores than those could be done by the ATOMS survey, and to detect previously unrevealed fainter filamentary structures. The spectral windows cover transitions of species including CO, SO, N_2D^+, SiO, $H_{30}\alpha$, H_2CO, CH_3CN, and many other complex organic molecules, tracing gas components with different temperatures and spatial extents. QUARKS aims to deepen our understanding of several scientific topics of massive star formation, such as the mass transport within protoclusters by (hub-)filamentary structures, the existence of massive starless cores, the physical and chemical properties of dense cores within protoclusters, and the feedback from already formed high-mass young protostars.

Key words: stars: formation – stars: kinematics and dynamics – ISM: clouds – ISM: molecules

1. Introduction

As the principal sources of heavy elements and UV radiation, high-mass stars ($M > 8\ M_\odot$) play a major role in the evolution of galaxies. However, the formation mechanism of high-mass stars is still under intense debate (e.g., Zinnecker & Yorke 2007; Pineda et al. 2023). A variety of models have been proposed, contending with each other or focusing on different aspects of high-mass star formation. Early models

disagreed about how a massive protostar obtains its initial mass and subsequently accretes additional mass. The competitive accretion scenario (e.g., Bonnell et al. 2004; Bonnell & Bate 2006) assumed initial fragmentation of a molecular cloud into low-mass cores each with mass approximately equal to the thermal Jeans mass. In contrast, the "turbulent core accretion model" (e.g., McKee & Tan 2003) suggested that high-mass stars form directly from turbulent massive gas cores. These idealized models depict protostars forming and accreting from their natal gas reservoirs which are treated as unstructured and obeying isotropic dynamics. Therefore, models that explained the presence of star-forming regions in/on hierarchical structures, or more specifically filamentary structures, were put forward (e.g., the global hierarchical collapse model, the inertial-inflow model; Heitsch et al. 2008; Vázquez-Semadeni et al. 2009; Padoan et al. 2020). These models were partly supported by the observations of far-infrared dust continuum by the *Herschel* space observatory and other ground-based single-dishes, which demonstrated that filaments are ubiquitous and closely correlated with star formation in nearby molecular clouds as well as massive clumps in the Galactic Plane (e.g., André et al. 2010; Könyves et al. 2015; Li et al. 2016; Liu et al. 2018, 2021b; Kumar et al. 2020; Schisano et al. 2020; Ge et al. 2023; Hacar et al. 2023).

Observations show that high-mass stars are rare, and mostly born in massive clumps within the Galactic plane that are much denser than low-mass star-forming clouds (e.g., Schuller et al. 2009). Considering their large distances ($\sim$kpc) and high dust extinction, studies of those massive clumps need high resolution interferometric observations that can resolve their internal gas structures and kinematics. The Atacama Large Millimeter/submillimeter Array (ALMA) provides an opportunity to investigate the inner hierarchical structures of high-mass star-forming regions in great detail. There is growing evidence of the existence of filaments within massive clumps giving rise to hub-filamentary structures (HFSs; e.g., Peretto et al. 2013; Yuan et al. 2018; Kumar et al. 2022; Liu et al. 2023a; Morii et al. 2023; Yang et al. 2023). However, most of these have been the results of case studies. The "ALMA Three-millimeter Observations of Massive Star-forming regions" (ATOMS) survey (Liu et al. 2020a) observed 146 active star-forming regions with ALMA at Band 3 ($\lambda \sim 3$ mm), aiming to systematically investigate the gas distribution, stellar feedback, and filaments inside massive clumps. The ATOMS survey revealed, in a statistical way, that HFSs are common within massive clumps (Zhou et al. 2022). Case studies of HFSs based on the ATOMS survey (Liu et al. 2022a, 2022b; Xu et al. 2023b) confirmed that HFSs at scales from 0.1 pc to several pc play a key role in high-mass star formation, and the stellar feedback would in turn regulate the shapes and evolution of HFSs (e.g., Peretto et al. 2013; Kumar et al. 2022; Liu et al. 2023a). A higher-resolution ($\sim$1000 au) survey would enable to systematically establish whether the hierarchical structures

remain common down to a protocluster scale, and to provide for theoretical studies the observational constraints onto the detailed process of gas mass transport down to the protocluster scale.

Inspired by the ATOMS survey, we initiated the "Querying Underlying mechanisms of massive star formation with ALMA-Resolved gas Kinematics and Structures (QUARKS)" survey program at ALMA (PIs: Lei Zhu, Guido Garay, and Tie Liu). The QUARKS survey selected the densest kernels of the massive clumps in the ATOMS survey, forming an unbiased sample (139) of protoclusters, and observed them at Band 6 ($\lambda \sim 1.3$ mm) of ALMA with much improved angular resolution than the ATOMS survey. The QUARKS survey aims (1) to statistically investigate the star formation process (e.g., fragmentation, outflows, disks) within an unbiased sample of protoclusters, (2) more specifically, to explore how (hub-)filamentary structures feed individual protostars within protoclusters, (3) to investigate the physical and chemical evolution of dense cores, and (4) to study various feedback mechanisms within protoclusters.

In this paper, we present an overall description of the QUARKS survey. The paper is structured as follows: In Section 2, we introduce the source sample and ALMA observations of the QUARKS survey. In Section 3, we describe the data reduction processes of both the continuum maps and spectral cubes. In Section 4, a first look at Sgr B2(M), a source within the sample of this survey, is presented to check the data quality and to explore in a preliminary fashion how the data can be linked to some of the science objectives of the QUARKS survey. In Sections 5 and 6, we present more science topics that can be addressed by the QUARKS survey and compare the QUARKS surveys with other ALMA programs. A summary is provided in Section 7.

2. Sample and Observations

2.1. Sample

The QUARKS sample contains 139 protoclusters, selected as the densest kernels of high-mass star-forming regions revealed by the ATOMS survey (Liu et al. 2020a). Among the 146 sources of the ATOMS, two sources are low-mass clumps ($<15\ M_{\odot}$), four sources are dominated by extended H II regions with angular sizes larger than the primary beam at Band 6, and one source has no detection of continuum emission by ATOMS. The seven sources show no massive and compact kernels under the view of ATOMS and were thus excluded in the QUARKS sample. The ATOMS sources were selected as the bright sources ($T_b > 2$ K) of the CS $J = 2 - 1$ survey of Bronfman et al. (1996), a complete and homogeneous molecular line survey of UC H II region candidates in the Galactic plane. The ATOMS sample was also observed in the SIMBA survey, a 1.2 mm continuum emission survey using the SEST telescope by Faúndez et al. (2004), and the survey of
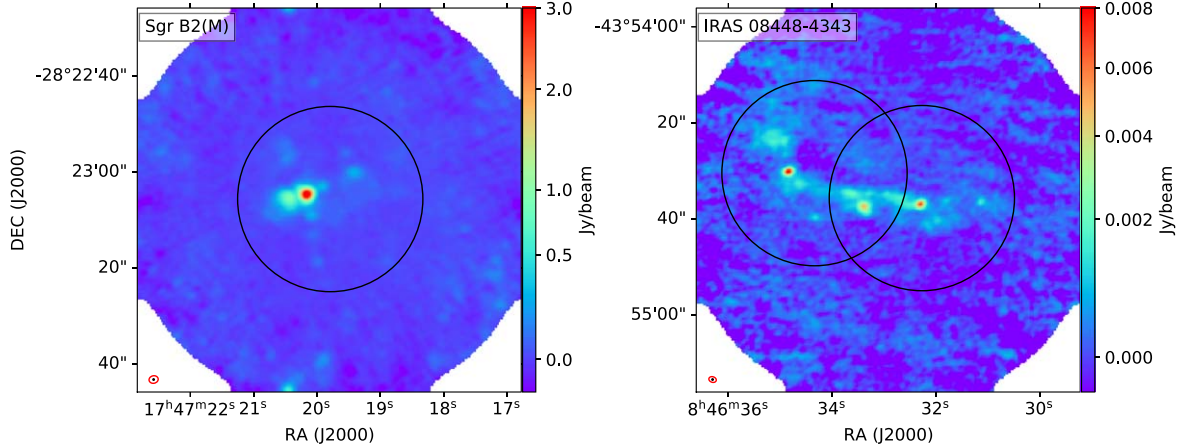
Figure 1. Example of the targets of the QUARKS survey. In each panel, the background is the Band 3 continuum of the ATOMS survey. The black circle is the primary beam of the ALMA 12 m array in Band 6. The red ellipse and the black dot in the lower-left corner show the angular resolutions of the ATOMS and QUARKS surveys, respectively.

HCN (4-3) and CS (7-6) using the ASTE telescope by Liu et al. (2016). The ALMA primary beam size at Band 6 is about 0.4 times the value in Band 3, hence the field of view (FoV) of the QUARKS survey can only cover part of the FoV of the ATOMS survey (Figure 1). For 17 sources with elongated and filamentary structures revealed by the 3 mm continuum emission of the ATOMS survey, two pointings for each were requested to entirely cover their dense kernels (e.g., IRAS 08 448-4343 as shown in the right panel of Figure 1). In total, QUARKS has 156 single-pointings to observe 139 proto-clusters. The clump masses (M_{clump}), quoted from Liu et al. (2020a), range from 40 to 2.5×10^5 $M_\odot$. These sources are located on the Galactic plane within a range of $|b| < 2°.1$ and $-98°.4 < l < 43°.8$, providing an unbiased sample of proto-clusters in the inner Galactic plane. For all the targets of the QUARKS survey, the target names and target centers (in both Equatorial and Galactic coordinate systems) are listed in Table A1.
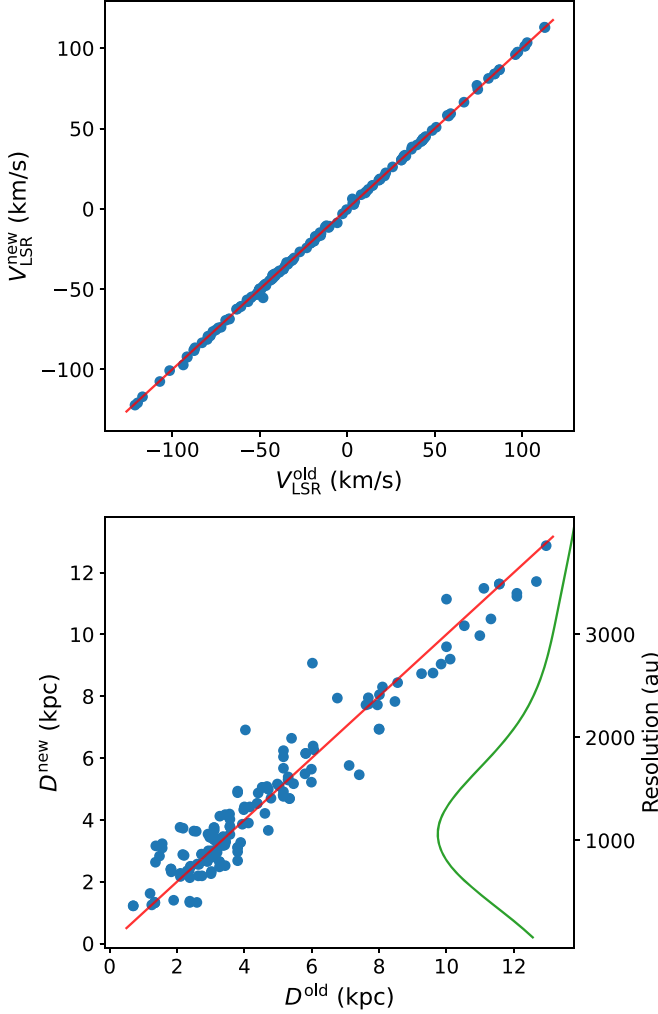
2.2. Re-evaluation of Sample Distance

The distances of the QUARKS sample (D^{old}) adopted by the ATOMS survey were initially derived from the velocities of CS $J = 2 - 1$ with an old Galactic rotation curve model (Bronfman et al. 1996). We updated the distances (D^{new}) using the distance calculator of Reid et al. (2016), based on the new systemic velocities of $H^{13}CO^+$ (V_{LSR}^{new}) measured from the ATOMS survey (Liu et al. 2020b). The distance calculator constrains the probability density function (PDF) of distance based on four types of information: kinematic distance (KD), the spiral arm model (SA), Galactic latitude (GL), and parallax source (PS) with different weights, which were assumed to be 0.85, 0.15, 0.85, 0.15, respectively (Reid et al. 2016). The velocities and distances of the sample are listed in Table A1.

As shown in Figure 2, V_{LSR}^{old} and V_{LSR}^{new} are consistent with each other, and the standard deviation of their differences is ~ 1 km s^{-1}, much smaller than the virial velocity (σ_{vir}) of ~ 5 km s^{-1} of giant molecular clouds (Chevance et al. 2023). Thus, the new calculated distance should not be influenced much by the new velocity employed. Moreover, we compared D^{new} and D^{old}, and found that they are consistent with each other with a 1σ deviation of 0.7 kpc (Figure 2). The distribution of the QUARKS survey linear resolutions (estimated adopting an angular resolution of 0″.3; see Section 2.3) is shown as the green line in the lower panel of Figure 2. The distances (D^{new}) of the sample of the QUARKS survey range from 1.2 to 12.9 kpc. The median value of distances is 3.7 kpc, at which a linear resolution of 1100 au can be achieved. The resolutions for most sources are within the range of 500–2000 au (Figure 2).

2.3. ALMA Observations

We conducted single-pointing observations for the 156 targets of the QUARKS survey using the ALMA. The observations started from late 2021 October (Project IDs: 2021.1.00095.S, 2022.1.00298.S, and 2023.1.00425.S; PI: Lei Zhu) with both the Atacama Compact 7 m Array (ACA) and the 12 m array of the ALMA at Band 6. Observations with the ACA were completed in late 2022 May. Observations with the 12 m Array have been partly executed in Cycles 8 and 9 and are expected to be completed in ALMA Cycle 10 (from 2023 October to 2024 September).

For each source, observations in three different ALMA configurations were proposed. The observations in low, moderate and high resolution configurations were conducted by the ACA, ALMA 12 m array C-2 and C-5 configurations, respectively. In the ACA, C-2 and C-5 observations, the on-source time for one

Table 1
ALMA Configurations of the QUARKS Survey

Configuration[a]	Resolution (arcsec)	MRS (arcsec)	rms_{line}[b] (mJy beam^{-1})
ACA	4.5	27	40
12 m array C-2	1	9	6
12 m array C-5	0.25	3.5	4
combined	0.3	27	3

Notes.
[a] For a small fraction of the sources, the moderate-resolution observations were conducted by C-3 (instead of C-2) configuration, and the high-resolution observations were conducted by C-6 (instead of C-5) configuration.
[b] The precise values of the line sensitivities (rms_{line}) of different sources vary by $\sim$50 percent because of factors such as the integration time and calibration.

Figure 2. Comparison between $V_{\text{LSR}}^{\text{new}}$ and $V_{\text{LSR}}^{\text{old}}$ is shown in the upper panel and between D^{new} and D^{old} (Lower) in the lower panel. The red lines represent $y = x$. The green curve represents the kernel distribution estimation of the source distances (with respect to the left Y-axis) or of the Band-6 spatial resolution (with respect to the right Y-axis) of the QUARKS sample.

1 cm^2 g^{-1} at 1.3 mm (Ossenkopf & Henning 1994), and a gas-to-dust mass ratio of 100. The angular resolutions of the combined images are typically better than 0.″35, which is about one-sixth of the resolution of the ATOMS survey (typically better than 2″) in Band 3 (Liu et al. 2020a). The significantly improved angular resolution of the QUARKS survey enables us to resolve dense cores, including massive starless core candidates and protostellar ones (star-forming dense cores, hot molecular cores, and UC H II regions) within protoclusters, down to a physical scale of 3500 au in the most distant sources at a distance of $\sim$10 kpc. For sources at a distance smaller than 3 kpc, the QUARKS survey can achieve a linear resolution better than 1000 au, and thus enable us to search for massive disk candidates (e.g., Johnston et al. 2015; Chen et al. 2016; Olguin et al. 2022).

The observations employed the Band 6 receivers in dual-polarization mode. Four spectral windows (SPW 1–4) were configured, and the frequency setups are shown in Table 2. The second, third, and fourth columns of Table 2 list the central frequency, bandwidth, and velocity resolution (δV) of each SPW (column 1). For the observations of the 12 m array and the ACA, each of the four SPWs has a bandwidth of 1.875 GHz and 2 GHz, respectively. The 5th to 7th columns of Table 2 list the parameters of the main transitions covered by each SPW, including the species name, transition labels, and upper-level energy (E_{u}). The four SPWs were configured to cover some commonly used lines including tracers for ambient gas (e.g., CO, ^{13}CO, C^{18}O), cold gas (N$_2$D$^+$), filament and infall (e.g., HC$_3$N), hot core (e.g., CH$_3$OH, C$_2$H$_5$CN, NH$_2$CHO), ionized gas (H30α), shocked gas (e.g., SiO, SO, H$_2$CO), and massive protostellar disk (CH$_3$CN), as listed in Table 2. SPW4 does not cover any low-energy strong lines (with upper-level energies $E_u < 100$ K) and thus is good for measuring the continuum emission. The Band 6 continuum is mainly produced by dust emission. However, the Band-3 continuum emission of the ATOMS survey arises from a blend of thermal dust emission and free–free emission from ionized gas (Zhang et al. 2023a).

science target was approximately 5, 1, and 5 minutes, respectively. The typical values of the angular resolution, maximum recovering scale (MRS), and the sensitivity of spectral lines (rms_{line}) for different configurations, including the combined configuration, are summarized in Table 1. The continuum sensitivity (rms_{cont}) is not listed, because the rms_{cont} of the combined data varies in a wide range from 0.1 to several mJy beam^{-1} for different sources, mostly because of the phase calibration and dynamic range limitations. Self-calibration was conducted for sources containing strong continuum (with peak value $\gtrsim$50 mJy beam^{-1}) cores (Section 3). We note that for 1.3 mm continuum 1 mJy beam^{-1} corresponds to a gas mass of 0.3 $M_\odot$ at a distance of 5 kpc, derived assuming a median dust temperature of 30 K, a dust opacity per unit dust mass of

<div align="center">

Table 2
Set up of the Spectral Windows and the Main Targeted Lines in the QUARKS Survey

</div>

SPW	f_{center} (GHz)	Bandwidth[a] (GHz)	δV (km s^{-1})	Species	Trans.[b]	E_u (K)	Note
SPW1	217.918 429	1.875	1.344	SiO	5-4	31.2	Jet/shock/outflow tracer
				H_2CO	3-2	20–68	Temperature/infall/outflow tracer
				HC_3N	24-23	131	Infall/dense-gas/filament tracer
				CH_3OH	4_2–3_1	45.5	Tracer of temperature/COMs
SPW2	220.318 632	1.875	1.329	$^{13}CO/C^{18}O$	2-1	16	Filament/outflow tracer
				CH_3CN	12-11	>68	Hot-core/massive-disk tracer
				SO	6-5	35	High-density/shock/outflow tracer
SPW3	231.369 566	1.875	1.266	CO	2-1	16.6	Ambient-gas/outflow tracer
				N_2D^+	3-2	22.2	Cold-gas tracer
				^{13}CS	5–4	33.3	Ambient gas/filament tracer
				H^{+c}	$H_{30}\alpha$		Ionized-gas/HII-region tracer
SPW4	233.519 748	1.875	1.254	NH_2CHO	11-10	>94	Hot-core tracer
				C_2H_5CN	26-25	>100	Hot-core tracer
				SO_2	…[e]	>200	Tracer of sulfur-rich hot gas
				Continuum[d]			Dust tracer

Notes.
[a] The bandwidths listed here are for the 12 m array observation. The bandwidth of each SPW of the ACA observations is 2 GHz.
[b] The transitions of C_2H_5CN, NH_2CHO, and CH_3CN referred to line groups. The H_2CO has more than one transition in SPW1. For these species, the ranges of E_u are listed.
[c] $H_n\alpha$ is the transition of H atom but traces H^+ (e.g., Gordon & Sorochenko 2002; Liu et al. 2023b).
[d] The SPW4 lacks low-energy lines and thus is good for extracting continuum emission (Section 3.2) and tracing hot cores (see Section 4.2).
[e] Transitions of SO_2 such as $16_{6,10}$–$17_{5,13}$ and $28_{3,25}$–$28_{2,26}$ are covered by the SPW4.

Combining the data of the QUARKS and ATOMS surveys, the dust emission and the free–free emission can be partly decoupled.

The channel widths of the four SPWs are 976.563 kHz, corresponding to a δV of 1.25–1.35 km s^{-1}, depending on the rest frequency. The spectral resolution is better than that of the two wide-band SPWs (SPWs 7 and 8) of the ATOMS survey, $\sim$1.6 km s^{-1} (Liu et al. 2020a). The velocity resolution of the QUARKS survey is high enough to spectrally resolve the emission lines of the outflows and ionized gas whose line wings or line widths are typically larger than 10 km s^{-1} (Liu et al. 2021a, 2022c; Zhang et al. 2022), and the emission of complex organic molecules (COMs) from hot cores ($\Delta V \sim$ 5 km s^{-1}; Qin et al. 2022; Taniguchi et al. 2023). The velocity gradients along the longest branches of HFSs were systematically revealed in the ATOMS survey to be 8.7 km s^{-1} pc^{-1} on average (Zhou et al. 2022), corresponding to a velocity difference of $\sim$5 km s^{-1} at the maximum recovering scale (0.6 pc at a distance of 5 kpc) of the QUARKS survey. Thus, spectral lines of species such as HC_3N can be used to trace the multi-scale structures and gas kinematics within the clumps (Liu et al. 2022a; Xu et al. 2023b). The massive starless core candidates found so far tend to show no emission lines or narrow lines (with linewidths <1 km s^{-1}) of cold gas tracers at Band 6 (e.g., Cyganowski et al. 2014; Kong et al. 2017). The N_2D^+ data of the QUARKS survey do not have sufficient spectral resolution to fully resolve the internal gas kinematics

of possible massive starless cores found by this survey, but can provide us the spatial distribution of cold gas. The line widths of the (sub-)Keplerian disks around massive stars are typically 5–10 km s^{-1} (Johnston et al. 2015; Chen et al. 2016; Sanna et al. 2019). The velocity resolution of the QUARKS survey is high enough to spectrally resolve the massive disks, if detected. In a word, for most purposes, the spatial and spectral resolution in the QUARKS survey should be high enough for resolving the gas structures and kinematics in massive protoclusters.

3. Data Reduction

The 12 m array data and the ACA data of the QUARKS survey were combined to reveal both compact and extended emission. Sgr B2(M), also named I17441-2822 in this survey, is one of the QUARKS sources with most complex and richest line emission. It is very complicated to reduce the data and produce high-quality images for this object. In this work, we take Sgr B2(M) as an example for evaluating our data reduction procedure. The imaging was carried out using the CASA software package of version 6.5 (McMullin et al. 2007).

3.1. Flagging of Emission Line Channels

To separate the emission of continuum and spectral lines, the emission line channels need to be flagged. The spectral lines mainly contain the extended strong emission (e.g., the transitions with $E_u < 100$ K listed in Table 2) and the forest

of COM lines from hot cores. First, we identified all the transitions of strong lines within the four SPWs through matching the ALMA pipeline reduced data cubes and the laboratory databases for spectral lines (e.g., the CDMS; Müller et al. 2001). Since $V_{\rm LSR}$ of the source is already known (Section 2.1), the observed frequencies of those strong lines can be roughly determined. Because of the possible existence of multiple velocity components and of foreground absorption, an aggressive strategy was adopted for strong lines by flagging out all the channels within $\pm 50\,{\rm km\,s^{-1}}$ of them.

For the line forest in hot cores, we first checked the fits cube of the ALMA pipeline products of the C-5 data, and manually extracted the spectra of hot cores. We calculated the rms of the unflagged channels, and then channels with intensity greater than $5\times$ rms were flagged in our reduction. This procedure is repeated until we can no longer flag any more channels. Since the influence of the line forest is limited to hot cores, a relatively conservative strategy was adopted by flagging out the channels of $\pm 10\,{\rm km\,s^{-1}}$ around those lines. For a source with no fits cube produced by the ALMA pipeline, the channel flag of Sgr B2(M) was adopted as a template flag. We shifted the template flag before applying it to other sources according to their velocities (Table A1). If the image quality of a source is not good because of an improper flag of emission line channels, we update the flag through checking the hot-core spectra extracted from its fits cube obtained in the first round of imaging and then conducted a second round of imaging.

3.2. Imaging and Self-calibration of Continuum Data

To increase the sensitivity of the continuum image, data of all the four SPWs were used. The line-free channels (channels that have not been flagged out by the procedures described in Section 3.1) of both the ACA and 12 m array data were fed to CASA-*tclean* to make the continuum maps. The Multi-scale Multi-Frequency Synthesis (mtmfs; McMullin et al. 2007) with an *nterm* of 2 was chosen as the deconvolving algorithm. This algorithm is appropriate for cleaning on the combined visibility data of multiple configurations and multiple SPWs. The *briggs* weighting with a *robust* of 0.5 was adopted. For a source with strong continuum emission such as Sgr B2(M), self-calibration is necessary to improve the image quality (Section 3.2.1). For a source observed by two pointings such as the IRAS 08 448-4343 (see Figure 3), we combined the visibility data of the two pointings before imaging.
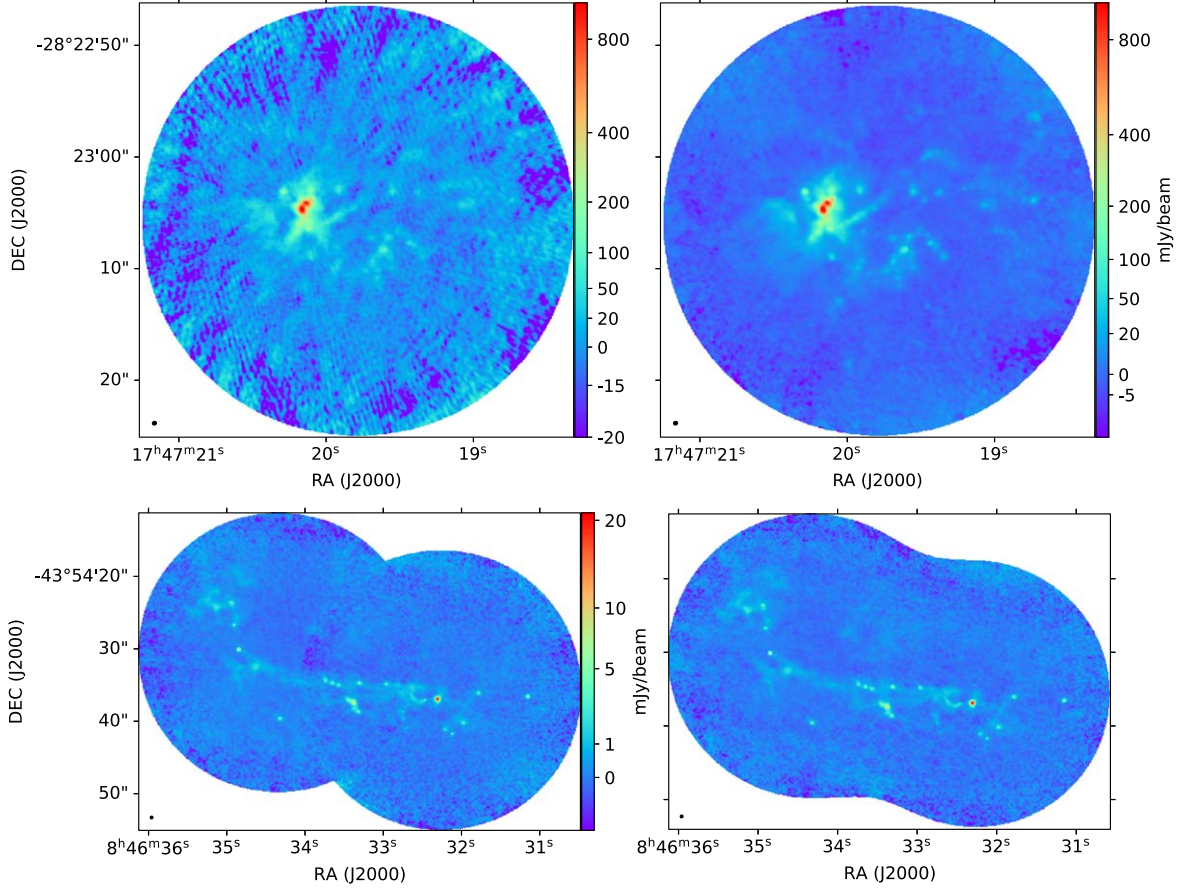
3.2.1. Self-calibration of Sgr B2(M)

The 1.3 mm continuum of the Sgr B2(M) is very strong with a peak intensity ($I_{\rm peak}$) of $\sim 1.2\,{\rm Jy\,beam^{-1}}$ and a total flux of >23 Jy. A threshold of 20 mJy beam^{-1} was adopted for the first iteration of the cleaning process of the continuum image. A lower threshold resulted in divergence. With that threshold, the reduced 1.3 mm continuum image of Sgr B2(M) show apparent

fuzzy artifacts (left panel of Figure 3). This result agrees with a low dynamic range ($I_{\rm peak}/{\rm rms_{cont}} \sim 180$) for sources having complicated and strong continuum emission, implying that the systematic errors of the calibrations of phase and amplitudes dominate over the thermal noise. Self-calibration is a technique for correcting the visibility phases and/or amplitudes of a source by comparing the visibility data with a model of the source itself (e.g., Richards et al. 2022). For strong continuum sources like Sgr B2(M), self-calibration must be applied to improve its dynamic range.

The phases of the visibility data were self-calibrated based on the model of the first round of cleaning, following the CASA manual.[23] A *solint* of 20 s was adopted for the *gaincal* task. Adopting a lower threshold (5 mJy beam^{-1} for Sgr B2(M)), the continuum image was cleaned in the second round, and the model was updated accordingly. Then, both the phases and amplitudes of the visibility data were self-calibrated based on the updated model. Finally, adopting an even lower threshold (1.5 mJy beam^{-1} for Sgr B2(M)), the cleaning process was conducted again to obtain the final continuum image. An rms of the residual map of 0.5 mJy was achieved through self-calibration for Sgr B2(M), corresponding to a dynamic range of greater than 2000. The final self-calibrated image greatly improves the quality compared with the non self-calibrated image. Extended structures that can only be marginally seen in previous observations (Figure 4) can be clearly recognized in the self-calibrated continuum image of the QUARKS survey, e.g., the north arc of Sgr B2(M) marked by the red rectangle in Figure 5 (see Section 3.2.2 for the discussion about the reliability of this structure). Approximately a hundred cores or compact substructures can be identified in Sgr B2(M) from the Band 6 self-calibrated continuum image of this survey (see Figure 5 and Section 4.1 for details). Note that some of compact cores have weak continuum emission, which will be carefully scrutinized below for their reliability (see Section 3.2.2).

There is no general rule for choosing the thresholds of self-calibration, and we conducted self-calibration manually and iteratively to optimize the thresholds that can avoid divergence while yielding good sensitivity. The continuum sensitivity of the QUARKS survey was expected to be 0.06 mJy beam^{-1}, according to the proposed observation design (Section 2.3). The final threshold of the continuum image of Sgr B2(M) is still higher than the expected sensitivity, mostly because (1) emission of Sgr B2(M) in Band 6 is dominated by strong spectral lines and thus the selection of line-free channels is difficult; (2) possible contamination comes from antenna sidelobes; (3) the strong and complex emission of Sgr B2(M) does not allow the self-calibration to further improve the dynamic range. Here we have conducted only two rounds of

---

[23] https://casaguides.nrao.edu/index.php?title=First_Look_at_Self_Calibration_CASA_6

Figure 3. The ALMA Band 6 continuum of Sgr B2(M) (upper) and IRAS 08 448-4343 (lower). For Sgr B2(M), the upper right and upper left panels are the images with and without self-calibration, respectively. For IRAS 08 448-4343, the lower left panel shows the image stitched from two independently cleaned images, and the lower right panel shows the image cleaned from the combined visibility data. The two lower panels share the same color bar. In each panel, primary beam correction has been applied, and the black small ellipse in the lower-left corner represents the synthesized beam.

self-calibrations and additional rounds with more carefully chosen thresholds may further improve the image quality. For a weak source, such as I08448-4343, a final threshold of 0.2 mJy beam^{-1} can be achieved without self-calibration, approaching the proposed 3σ sensitivity, and thus self-calibration is not required for it (lower panels of Figure 3).

3.2.2. Reliability of the Self-calibration

To evaluate the reliability of our self-calibration, we examined the self-calibrated continuum image of Sgr B2(M) from the QUARKS survey through comparing it with observations from different frequency bands (Figure 4). Sgr B2(M) was observed with ALMA at Band 6 by SM17 (Sánchez-Monge et al. 2017) in Cycle 2, with a resolution of $\sim0\rlap{.}''4$, similar to the resolution of the QUARKS survey of $\sim0\rlap{.}''3$. However, the sensitivity of SM17 is 8 mJy beam^{-1}, which is about 16 times lower than that of the QUARKS survey for Sgr B2(M) (~0.5 mJy beam^{-1}). The peak intensities of the

Band 6 continuum of Sgr B2(M) are about 1.8 and 1.2 Jy beam^{-1} by SM17 and QUARKS, respectively, and are consistent with each other considering the different beam sizes and frequencies. All the cores of Sgr B2(M) identified by SM17 can be successfully recognized in the QUARKS continuum map (Section 4.1).

Two isolated cores, numbered 55 and 96 in Figure 5, are visible in the self-calibrated continuum map of the QUARKS survey, but would be overwhelmed by noise if self-calibration were not applied (Figure 3). These cores are not visible in the continuum map of SM17 (see panel (b) of Figure 4), but are present in the ALMA Band 3 ($\lambda\sim3$ mm) continuum map observed by Ginsburg et al. (2018) with signal-to-noise ratios (S/Ns) greater than 5 at a resolution of $\sim0\rlap{.}''5$ (see panel (a) of Figure 4). The long-baseline Band-6 observations by Budaiev et al. (2023) have also revealed these two cores at an angular resolution of $\sim0\rlap{.}''06$. Thus, these two cores seen in the self-calibrated continuum map of the QUARKS survey should be reliable.
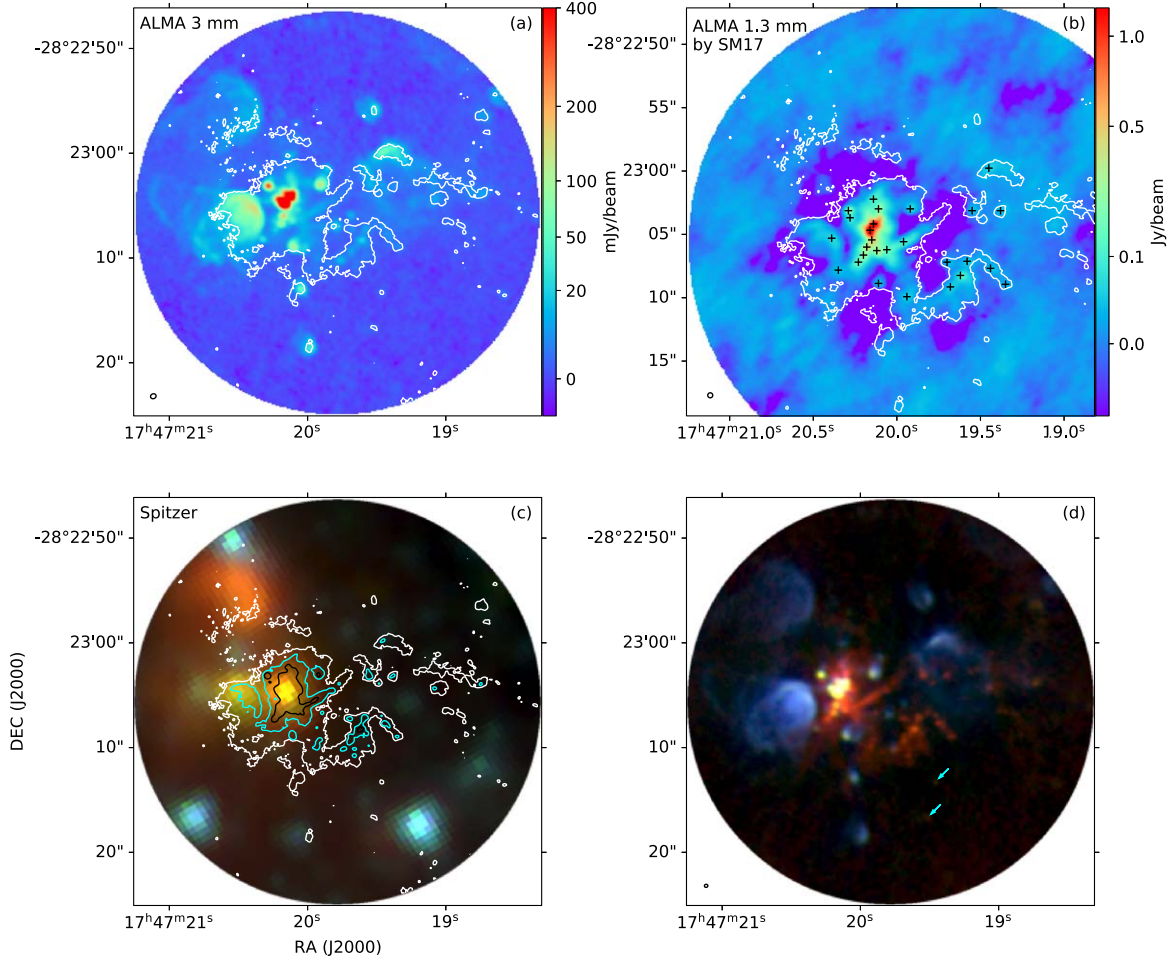
Figure 4. (a) Image of the ALMA Band 3 continuum emission of Sgr B2(M) with a resolution of $\sim0''5$ by Ginsburg et al. (2018). The beam size is shown as an ellipse at the lower-left corner. The white contour shows the ALMA Band 6 (at 1.3 mm) continuum emission from the QUARKS survey at the level of 5σ (2.5 mJy beam^{-1}). (b) Image of the ALMA Band 6 continuum emission from SM17 (Sánchez-Monge et al. 2017). The fields of view of SM17 and the QUARKS survey are not identical, but all 27 cores identified by Sánchez-Monge et al. (2017) marked by the black crosses are shown in this panel. The contour is the same as in panel (a). Note that the color map (*rainbow* with a power-law normalization with a power index of 0.4) is similar to that of Figure 3, where the ALMA Band 6 continuum of the QUARKS survey is shown. (c) Three-color image composed by the Spitzer 8 (red), 4.5 (green), 3.4 (blue) μm continuum. The white, cyan, and black contours show the ALMA Band 6 continuum of the QUARKS survey, at the levels 2.5, 15, and 50 mJy beam^{-1}, respectively. (d) Three-color image composed of the ALMA Band 6 continuum of the QUARKS survey in red, the ALMA Band 3 continuum by Ginsburg et al. (2018) in green, and the VLA Band C (at ~6 GHz) continuum by Meng et al. (2022) in blue. The cyan arrows pinpoint Cores 55 and 96 (see Figure 5 and Section 3.2.2). The beam size of the QUARKS survey is shown as an ellipse at the lower-left corner.

Core 97, with a weak peak intensity of 5 mJy beam^{-1} at Band 6 measured from the self-calibrated continuum image of the QUARKS survey, is located near the central crowded regions of Sgr B2(M). This core is not visible on the continuum map of SM17, but can be seen on the ALMA Band 3 (Ginsburg et al. 2018) and VLA Band C (6 GHz; Meng et al. 2022, see also panel (d) of Figure 4) continuum maps. Therefore, core 97 is considered reliable and could be an embedded UC H II region.

The north arc marked as a red rectangle in Figure 5 has not been reported previously. We checked the 3 mm continuum (Ginsburg et al. 2018) and the 1.3 mm continuum (Sánchez-Monge et al.

2017) from earlier observations and found tentative detection of the north arc (Figure 4), confirming its reliability. In conclusion, most, if not all, compact cores and extended structures in the continuum emission of the QUARKS survey can be reliably recovered by self-calibration in our data reduction.

3.3. Spectral Cube

The calibration tables calculated from the self-calibration of continuum data were applied to all the channels, including the emission line channels. Subsequently, polynomial fitting was conducted to the data of the line-free channels in the visibility
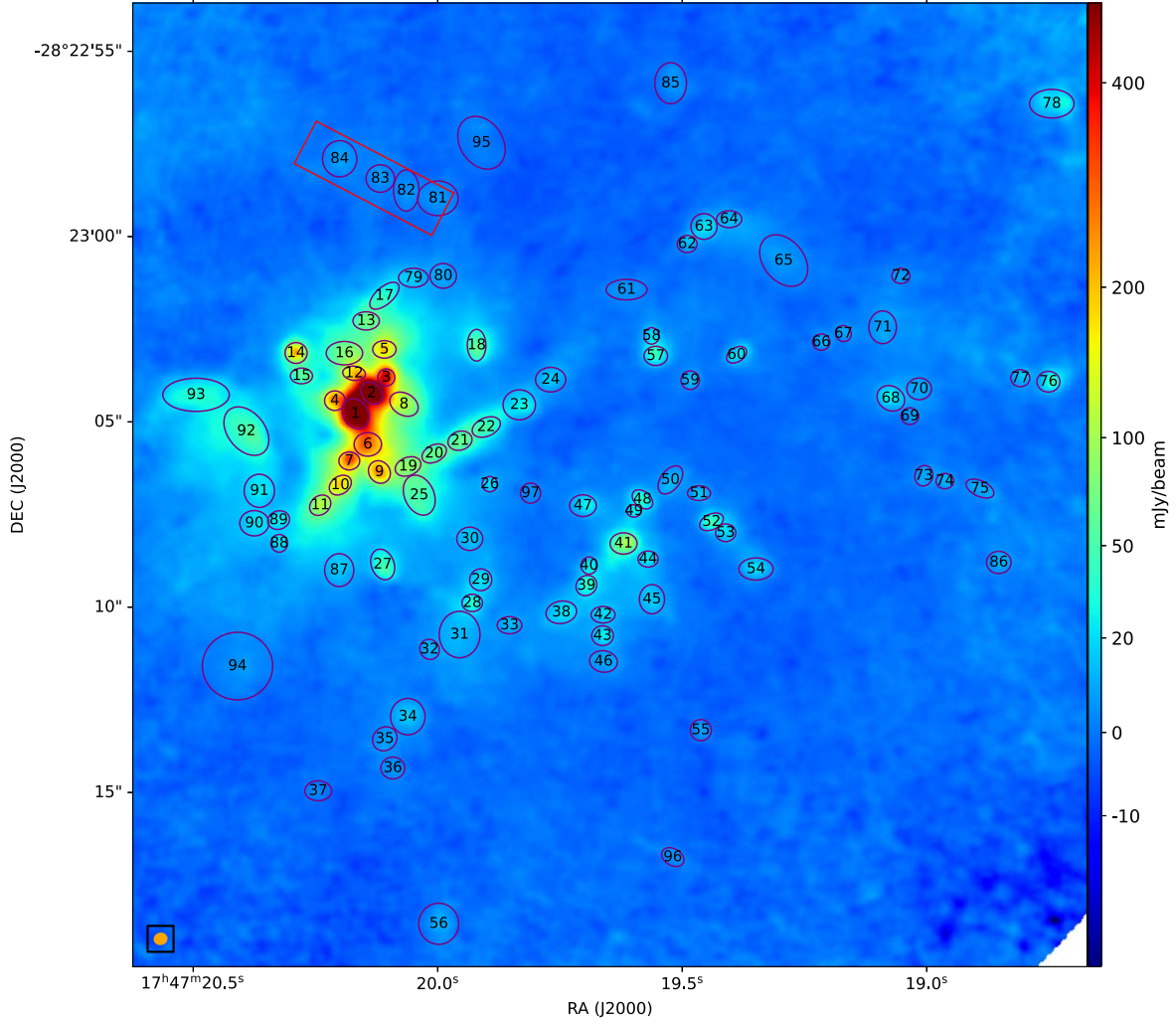
Figure 5. Zoom in the image of the right panel of Figure 3. The purple ellipses and black numbers marked the cores and substructures of Sgr B2(M) detected in the Band-6 continuum image (Section 4.1). The red rectangle marks the north arc of the Sgr B2(M). The orange ellipse in the lower-left corner represents the synthesized beam size.

domain, and the continuum components were subtracted using the *uvcontsub* task of CASA. The visibility data of each SPW were then fed to CASA-*tclean* to generate cube of spectral lines. Thus, all the spectral cubes we generated are continuum-subtracted. The deconvolution algorithm of *tclean* was chosen as *multiscale*. Since the dynamic ranges of the spectral images are overall lower than that of continuum images, in practice, a uniform threshold of $15\,\mathrm{mJy\,beam^{-1}}$ (corresponding to a brightness temperature, T_{b}, threshold of 3.8 K for a beam size of $0\rlap.''3$) was chosen to optimize the performance of the cleaning of spectral cubes for most sources. As a result, the rms of the spectral cube of the QUARKS survey is $\sim 3\,\mathrm{mJy\,beam^{-1}}$ per channel, equivalent to an rms of T_{b} of 0.8 K per channel.

4. A First Look at Sgr B2(M)

The giant molecular cloud Sgr B2 is the most massive ($\sim 10^7\,M_\odot$; e.g., Goldsmith et al. 1990) region with ongoing high-mass star formation in the Galaxy. It is an exceptional region in the Central Molecular Zone (CMZ), which appears to be deficient in star formation (e.g., Guesten & Downes 1983; Kauffmann et al. 2017). Its distance, estimated from the newest version of the distance calculator of Reid et al. (2016), is 8.3 kpc (Table A1), consistent with the values adopted by previous studies (e.g., Ginsburg et al. 2018; Meng et al. 2019) based on the results of Reid et al. (2014). Sgr B2(M) is one of the two most well-studied "hot cores" (Sgr B2(M) and Sgr B2(N)) located in the central part of Sgr B2, which are actually
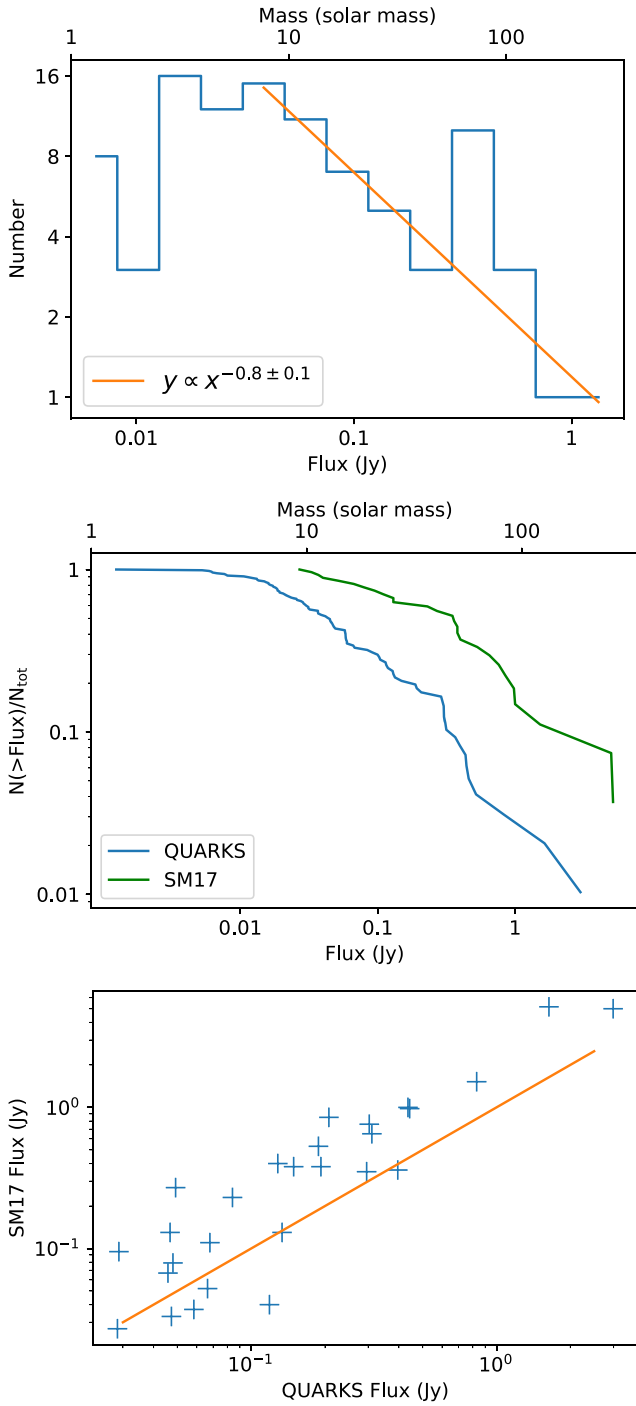
Figure 6. Upper: The fluxes distribution of the cores in Sgr B2(M) (Figure 5). The orange line represents the power-law fitting of data at the high-flux end. Middle: The cumulative fluxes distribution of the cores in Sgr B2(M) by QUARKS (blue) and SM17 (green; Sánchez-Monge et al. 2017). For reference, the corresponding mass estimate as the first order of approximation (Section 4.1) is displayed at the top axis of the upper and middle panels. Lower: Comparison between the core fluxes measured by QUARKS and SM17. The orange line represents $y = x$. Note that QUARKS detected more fragmented cores than SM17 because of better angular resolution and sensitivity (Section 4.1).

high-mass protoclusters containing hundreds of protostellar cores (Ginsburg et al. 2018; Möller et al. 2023). Sgr B2 has also provided the detection of most molecules discovered so far in the interstellar medium, and thus is considered a very good target for studying astrochemistry (e.g., Belloche et al. 2008; McGuire 2022). In this section, we explore the continuum (Section 4.1) and spectral (Section 4.2) data, and present some links between the data and science topics of the QUARKS survey through a brief case study of Sgr B2(M).

4.1. Mini-starburst in the Protocluster Sgr B2(M)

First, we manually identify the cores and core-like substructures in the continuum map using the image viewer CARTA.[24] The criteria of a core are (1) it should have peak intensity larger than 5σ; (2) it is isolated or the major part of its emission region should not merge into its neighboring cores. In total, 97 cores were recognized. We then fitted these cores using 2D Gaussian functions, using the optimization algorithm provided by the Python package, *lmfit*.[25] The catalog of the cores, including the position, FWHMs of the major (L_{maj}) and minor (L_{min}) axes, position angle (PA), peak intensity (I_{peak}), and integrated flux are listed in Table A2. The 1.3 mm observation of Sánchez-Monge et al. (2017) revealed 27 cores in Sgr B2(M), which are marked by the black crosses in panel (b) of Figure 4. We crosschecked the two core catalogs, and the results are listed in the last column of Table A2. All the cores of Sánchez-Monge et al. (2017) can be identified in the QUARKS continuum image. The QUARKS survey has better angular resolution and continuum sensitivity compared with that of Sánchez-Monge et al. (2017), and thus our survey is capable of resolving many smaller-scale cores and identifying more weak entities. For example, the cluster of protostars located in the southwest of the central part of Sgr B2(M), which cannot be well resolved by Sánchez-Monge et al. (2017), is revealed in our survey as a collection of grape-like cores. These cores may have evolved from a hub-filamentary structure, but their intrinsic characteristics are to be further explored.

The fluxes of the cores identified in the QUARKS continuum image range from 5 mJy to 1 Jy. Assuming a uniform dust temperature of 100 K (the typical value of Sgr B2(M) by Möller et al. 2023) and a gas-to-dust mass ratio of 100, this corresponds to a mass range of approximately 1–100 $M_\odot$. For the brightest two cores (i.e., Cores 1 and 2 having $I_{peak} \gtrsim 0.5$ Jy beam^{-1}), the optically thin assumption could underestimate the core mass. For the remaining cores, their peak fluxes correspond to peak brightness temperatures lower than 100 K, suggesting that their mass estimate could not be severely affected by that assumption. The total mass of the cores in Sgr B2(M) is 2800 $M_\odot$, yielding a mean mass of 30 $M_\odot$, much lower than the value of Sánchez-

---

[24] https://cartavis.org/
[25] https://pypi.org/project/lmfit/
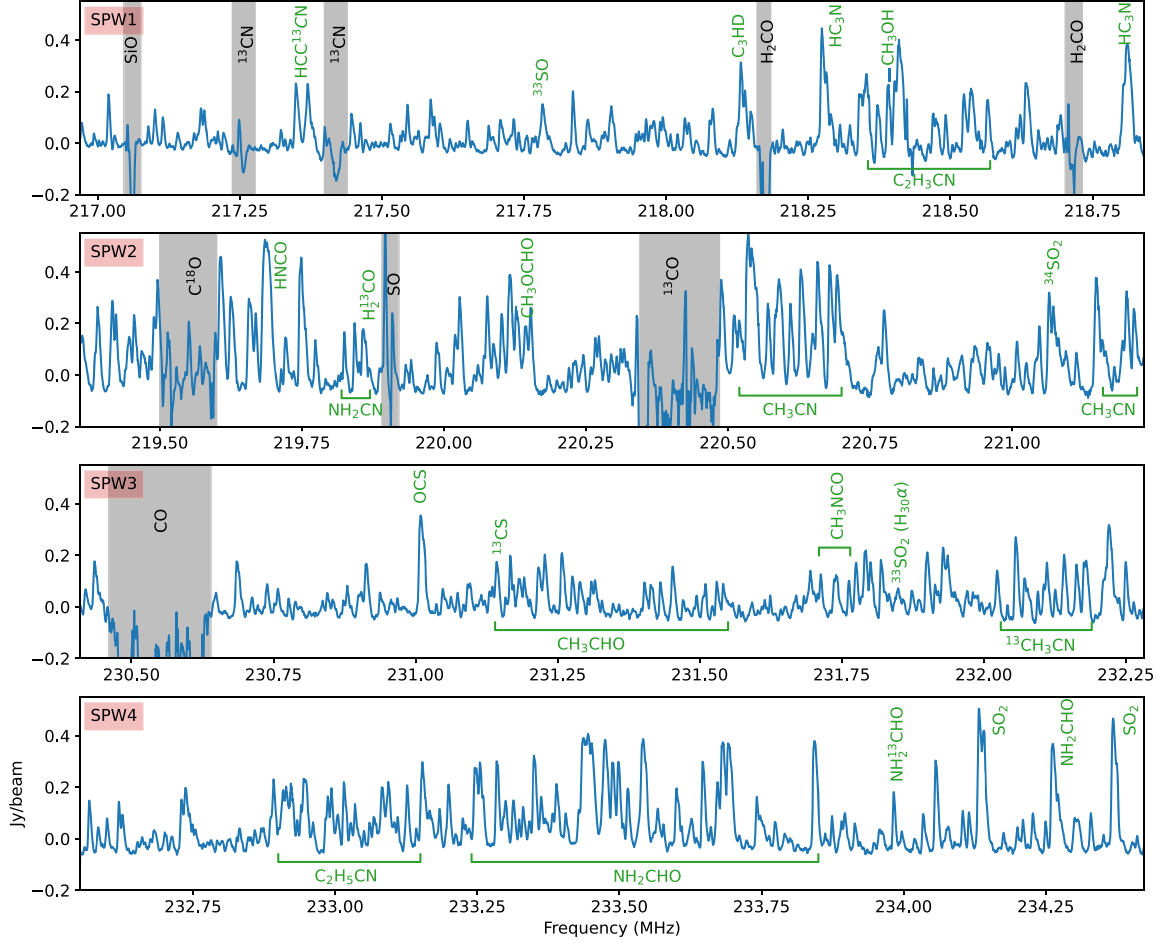
Figure 7. The QUARKS spectra of core 6, the line-richest core among those in Figure 5. The gray-shaded regions mark the strong lines showing absorption. The species of strong emission line or group of lines are labeled in green. Each of the labeled line groups is assigned to one species that dominates the spectral emission within the corresponding frequency range. The velocity (V_{LSR}) of core 6 is 67 km s^{-1}.

Monge et al. (2017) which is 150 $M_\odot$. This is expected since the QUARKS survey can probe smaller fragmented scales of Sgr B2(M) due to higher sensitivity. The high-mass ($>5\,M_\odot$) end of the core mass function (CMF) show a power-law distribution ($dN/d\log(m) \propto m^{-\alpha}$) with a power index of 0.8 ± 0.1 (Figure 6), implying a top-heavy shape as compared to the canonical initial mass function (Bastian et al. 2010; Sanhueza et al. 2019; Motte et al. 2022). The brightest cores may be even more massive if taking into account the effects of optical depths (Sánchez-Monge et al. 2017), which would result in a more top-heavy CMF. The kink in the high mass end result from the interference of dust shells of ionized regions (e.g., Cores 92 and 93 in Figure 5), which are extended and thus have relative large fluxes. The emission of the shells at 1.3 mm is probably highly contaminated by free–free ionized gas emission (Sánchez-Monge et al. 2017). The CMF of Sgr B2(M) is similar to that of Sgr B1-off, the mass range and power index of which are 0.3–230 $M_\odot$ and 0.83 ± 0.21, respectively (Lu et al. 2020). Note that Sgr B1-off is less evolved than Sgr B2(M), and a dust temperature of 20 K was adopted by Lu et al. (2020). These results may imply that the evolutionary tracks of the two regions may be regulated by some shared parameters of the environments, although the varying dust temperatures provide challenges for precisely deriving the core masses. On the other hand, the similarity of the CMFs between Sgr B2(M) and other high-mass star-forming regions (with $\alpha < 1$; e.g., Cheng et al. 2018; Lu et al. 2020; Pouteau et al. 2023) implies that the QUARKS is sensitive enough to find out most of the high-mass cores in Sgr B2(M). The core density of Sgr B2(M) is then derived to be $\sim$100 pc^{-2}. This value is much higher than the value (19 pc^{-2}) of the mini-starburst ridges of W43 (Pouteau et al. 2022, 2023), implying stronger mini-starburst activities in Sgr B2(M) compared with the W43 mini-starburst region, an analog of a forming super star cluster (Bally et al. 2010).

11
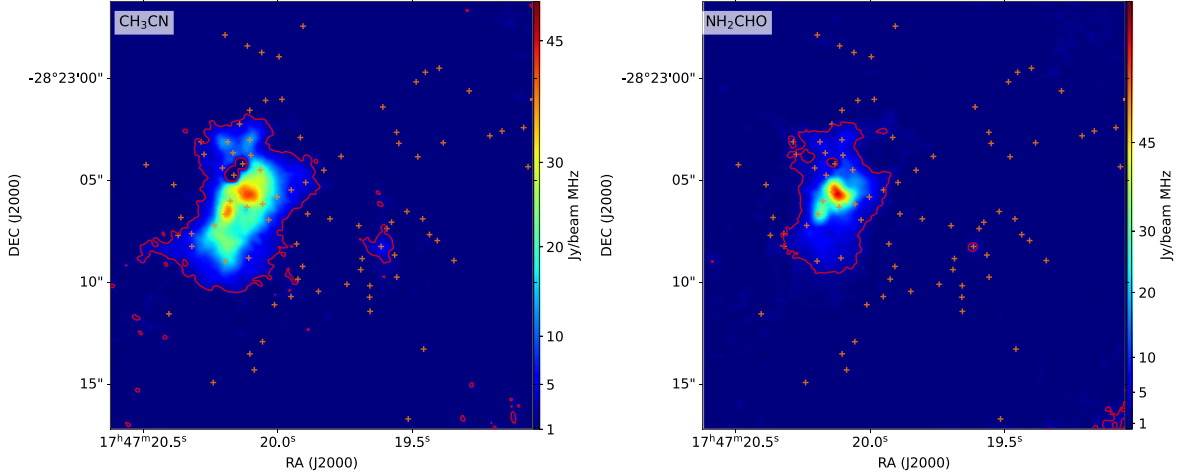
Figure 8. Left: The intensity map integrated from 220.52 to 220.7 GHz, which contains a line group of CH_3CN as shown in Figure 7. Right: The intensity map integrated from 233.24 to 233.85 GHz, which contains a line group of NH_2CHO. In each panel, the red contour is for the intensity map with a level of 2 Jy beam^{-1} MHz, and the orange crosses mark the continuum cores of this work.

4.2. COM-rich Hot Cores in Sgr B2(M)

Among the 97 cores, core 6 has the richest spectral line features (Figure 7). The spectra of core 6 are shown in Figure 7 as a gallery of the spectral lines that can be detected in the four SPWs of the QUARKS survey. Note that the spectra of core 6 do not contain all transitions that can be detected by the QUARKS survey. Some important lines listed in Table 2 cannot be seen in the spectra of core 6. For example, no broad ($\Delta V > 20$ km s^{-1}) line feature contributed by $H_{30}\alpha$ was detected. A weak and narrow ($\Delta V \sim 6$ km s^{-1}) line feature can be seen at a frequency close to that of $H_{30}\alpha$, and this line feature can be assigned to a transition of $^{33}SO_2$ through LTE fitting as described in Liu et al. (2022d). It implies that core 6 is a "pure" hot core and does not harbor a UC H II region that is detectable by the QUARKS survey based on the data of H30α. The emission of N_2D^+, a cold gas tracer, is also not detected in core 6, a COM-rich hot core.

We integrated the line groups of CH_3CN from 220.52 to 220.7 GHz and NH_2CHO from 233.24 to 233.85 GHz (see Figure 7), and the integrated intensity maps of the two line groups of Sgr B2(M) are shown in Figure 8. CH_3CN and NH_2CHO are both COM species, and the two line groups trace COM-rich hot gas. The emission of the two line groups is concentrated on a similar region, the central part of Sgr B2(M) with a size of $\sim8''$ (0.3 pc). Therefore, the central part of Sgr B2(M) can be treated as a single "big hot core". The molecular gas inside and among individual dense cores within this "big hot core" is all COM-rich hot gas. The line group of NH_2CHO is more centrally peaked than that of CH_3CN, implying different excitation states or chemical segregation within the "big hot core." The integrated intensity of the two line groups show another peak around core 41, which is more like a normal hot core heated by the massive protostars within it.

More than half of the continuum cores are not located within the COM-rich emission regions (Figure 8). Those cores can be divided into three types according to their spectral features, including (1) line-poor cores with no emission lines other than the strong lines of common species such as CO and ^{13}CS, (2) cores associated with H II regions showing strong emission of H30α, and (3) sulfur-rich cores with very strong emission of sulfur-bearing species such as SO, SO_2, and their isotopologues.

We show the spectra of cores 60, 93, and 84 in Figure 9 as examples of types 1, 2, and 3, respectively. Core 60 of this work is one of the 27 cores identified by Sánchez-Monge et al. (2017) in Sgr B2(M). Sánchez-Monge et al. (2017) treated all those 27 cores as hot cores. However, some of these cores, such as their core A23 (core 60 in this work), exhibit a deficiency in spectral lines. The dust temperatures of these 27 cores of Sánchez-Monge et al. (2017) span a range of 46–162 K, as reported by Möller et al. (2023), with core A23 having a dust temperature of 72 ± 38. Considering the diversity of dust temperatures, we classify cores with COM-rich line features as hot cores, specifically those enclosed within the red contours in Figure 8. The sulfur-rich cores also tend to have high temperatures but are mainly located on the faint north arc (Figure 5), with a very different spatial distribution compared with other gas components of Sgr B2(M) (X. Liu et al. 2023, in preparation).
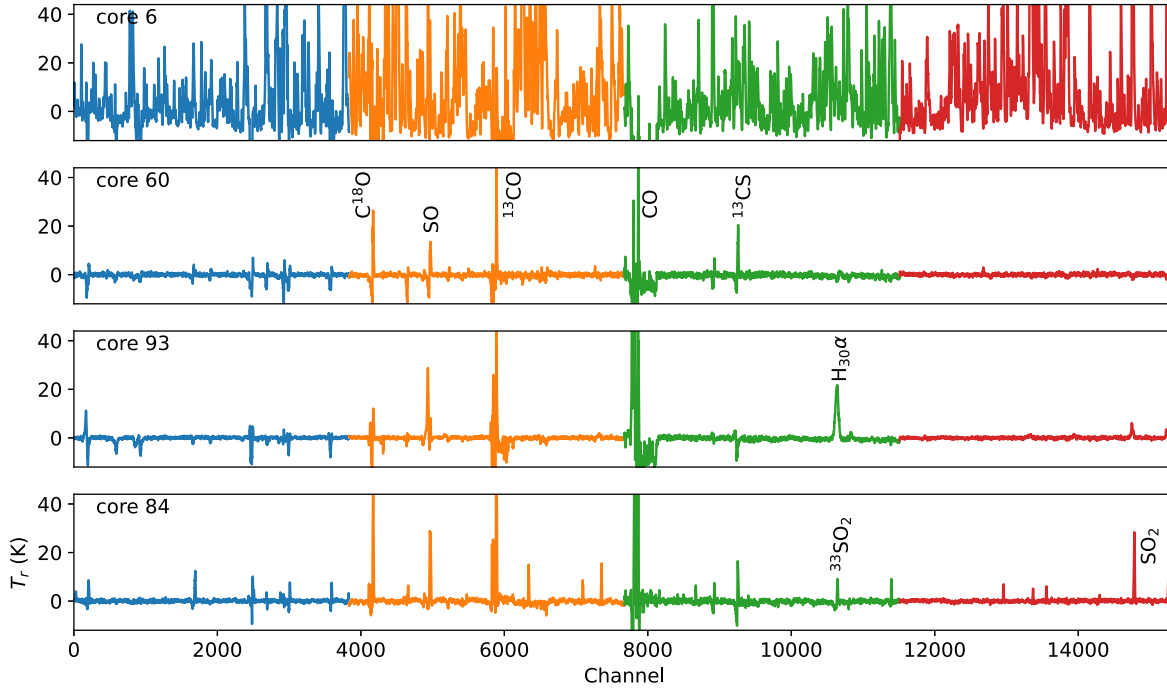
Figure 9. Example spectra of cores of different types (Section 4.2). The blue, orange, green and red lines are the spectra of SPWs 1–4. See Figure 5 for the locations of these cores. The spectra of hot core (core 6) is for comparison. The core 84 shows more than 20 lines of sulfur-bearing species. See Figures 7 for the zoom-in spectra of core 6.

5. Scientific Objectives of the QUARKS Survey

Some scientific objectives (such as fragmentation, core mass function, astro-chemistry) of the QUARKS survey have been briefly mentioned above (Section 4), through looking at an exemplar source, the Sgr B2(M). There are, however, more science topics that can be addressed by the QUARKS survey data but have not been fully discussed, as discussed below.

Hunting for massive starless cores is an important topic of this project. Whether or not massive starless cores exist serves as a key discriminator between star formation theories, but still in dispute (e.g., McKee & Tan 2003; Bonnell et al. 2004; Heitsch et al. 2008). However, hunting for high-mass starless cores has proven to be very challenging, and only a few promising candidates have been reported (e.g., Cyganowski et al. 2014; Wang et al. 2014; Kong et al. 2017). Most of the efforts in the search for massive starless cores have been focused on the early stages of massive clumps (e.g., infrared dark clouds). However, observations indicated that gas accretion inside protoclusters (e.g., through hub-filamentary structures) would continue before being destroyed by stellar feedback (e.g., Sanhueza et al. 2021; Zhou et al. 2022; Xu et al. 2023a). Several numerical simulations suggest that thermal feedback from OB protostars and the strong magnetic field of proto-stellar clusters can play a crucial role in reducing the level of fragmentation and producing massive dense cores (e.g.,

Krumholz et al. 2007; Offner et al. 2009; Myers et al. 2013). Thus, it is possible that the newly assembled gas within evolving protoclusters could form massive starless cores. During the pioneer exploration of the QUARKS data, we have found a massive starless core candidate in I18507+0121, which shows no emission lines except for the line of N_2D^+ (X. Mai et al. 2023, in preparation). The QUARKS survey can provide the high-mass star formation community additional samples of massive pre-stellar cores to explore.

How stellar feedback from outflows, H II regions and stellar winds from formed OB protostars influences the formation of new generation of stars and reshapes gas distribution in clouds is highly debated (e.g., Krumholz et al. 2014; Peters et al. 2017; Schneider et al. 2020; Zhang et al. 2023b; Herrington et al. 2023; Pouteau et al. 2023). The ATOMS survey studied the impact of UC H II regions (S. Zhang et al. 2023, in preparation) on their surrounding molecular gas, but detailed investigation was limited by sensitivity, and resolution. The high resolution of the QUARKS survey could help to study how the feedback of UC H II regions (traced by $H_{30}\alpha$) influence the surrounding star formation activities, e.g., the core masses under the impact of H II region on a scale of thousands au. The thermal feedback (e.g., shocks) from the ionized gas of the young H II regions could be reflected in the velocity and temperature distributions over the surrounding dense cores, which could be revealed by molecular transitions such as CH_3CN, CH_3OH and their

isotopologues (Moscadelli et al. 2018) . The outflow tracers such as ^{12}CO $J = 2-1$, ^{13}CO $J = 2-1$ and SiO $J = 5-4$ included in the QUARKS survey are very helpful for detecting molecular outflows and investigate the role of outflow feedback in maintaining turbulence (e.g., Li et al. 2020; Baug et al. 2021) or heating gas (Wang et al. 2012) in gas clumps.

For protocluster within 3 kpc, a resolution of better than 1000 au would enable us to search for massive disks (Chen et al. 2016) and large-scale ($>$10,000 au) gas streamers or spiral arms that may feed the disks (Pineda et al. 2020; Lee et al. 2023) with various gas tracers (e.g., CH$_3$CN, SO).

Simulations and recent observational studies revealed time-dependent co-evolution between clump and core masses (e.g., Bonnell et al. 2004; Sanhueza et al. 2019; Anderson et al. 2021; Xu et al. 2023a). The QUARKS survey would help to reveal the co-evolution between protoclusters and protostars in different environments. Species such as N$_2$D$^+$, H$_2$CO, CH$_3$CN, and SO$_2$ are good tracers of gas temperature ranging from 10's to hundreds Kelvin, enabling the QUARKS survey to investigate the evolution of cores in different stages and other substructures found inside protoclusters. We expect that the QUARKS survey can help the study of the co-evolution of the multi-scale structures of/within protoclusters, through case studies of typical sources, and, more importantly, through unbiased statistical studies.

6. Link to Other ALMA Large Survey Programs

High-resolution follow-up studies of the discoveries and investigations carried out in the ATOMS survey (Liu et al. 2020a) is an important goal of the QUARKS survey. How the protostars in protoclusters accumulate mass and in turn affect their natal clumps and regulate new star formation is an important topic for both projects. The ATOMS survey has revealed ubiquitous filaments as well as filament-hub systems (HFSs) in protoclusters from dense core scales ($\sim$0.1 pc) to clump/cloud scales ($\sim$1–10 pc), and has found evidences for filamentary accretion at all scales (Zhou et al. 2022). The QUARKS survey can be used to check whether HFSs will further fragment down to a scale of 0.01 pc, and can inspect how they feed individual protostars within protoclusters. The QUARKS survey could also be used to establish the sample of hot cores. The ATOMS survey found 60 hot cores, contributing so far the largest uniform sample of hot cores observed with similar angular resolution and spectral coverage (Qin et al. 2022). The QUARKS survey, with much higher resolution, will resolve these hot cores, and help to statistically study the chemical diversities of COMs and the evolution of hot cores.

Some large programs of ALMA, e.g., the ALMA-IMF (Motte et al. 2022) and ALMAGAL (PI: Sergio Molinari), have science goals similar to or overlapping with that of the QUARKS survey. Compared with those programs, the QUARKS survey has some unique advantages. The ALMA-IMF observed 15 extreme ($M_{\text{clump}} > 2500$ $M_\odot$) and nearby (2–5.5 kpc) protoclusters in mosaic mode at a spatial resolution of $\sim$2000 au, aiming to make breakthroughs in studying the origin of the initial mass function (IMF) of stars. The single pointing mode of the QUARKS survey enables to generate quickly observe a relatively larger (139) and unbiased (Section 2.1) sample of protoculsters. Guided by the observations of the ATOMS survey in Band 3 (Liu et al. 2020a), QUARKS focuses on the dense kernels of the protoclusters that harbour majority of the massive protostars. In Sgr B2(M), only 5 compact cores were detected by the ATOMS survey, and the number by the QUARKS survey is more than 15 times that value. In the weak-continuum source, IRAS 08 448-4343, more than 20 dense cores have been revealed by the QUARKS survey (Figure 3). The ATOMS survey identified 453 compact cores, and it is reasonable to expect that the QUARKS survey would detect at least 10 dense cores for each source on average and 1500 ones in total. The total bandwidth (7.5 GHz) of the QUARKS survey is twice the total bandwidth (3.75 GHz) of the ALMA-IMF. The wide bandwidth makes the QUARKS survey ideal for studying the chemical properties of individual protostars and of the protoculster as a whole, e.g., investigating the chemical differentiation between O- and N-bearing COMs (e.g., Wyrowski et al. 1999; Peng et al. 2022; Qin et al. 2022), and exploring the formation mechanisms for individual complex organic molecules (e.g., CH$_3$COCH$_3$ and CH$_3$CHO). The QUARKS survey can help to statistically study the properties of protostars in an unbiased sample of protoclusters, and thus fully investigate the CMF at the high-mass end in widely different Galactic environments and at different evolutionary stages, bined by distances and protocluster properties.

ALMAGAL observed more than 1000 dense clumps with $M > 500$ $M_\odot$ and $d < 7.5$ kpc with a linear resolution of $\sim$1000 au and a mass sensitivity of 0.3 $M_\odot$ at 1.3 mm, similar to the QUARKS survey. All the four SPWs of ALMAGAL are located within the frequency range of 216.9–221 GHz, corresponding to the SPWs 1 and 2 of the QUARKS survey. Emission lines of some important species, such as ^{12}CO and N$_2$D$^+$, and strong recombination lines (the α lines of hydrogen) were not covered by ALMAGAL. QUARKS covered the transtions of all the three isotologues of carbon monoxide (CO, ^{13}CO and C^{18}O), and in combination with the ATOMS survey, we can study the large-scale kinematics and structures up to 1 pc (30$''$ at a distance of 8 kpc). N$_2$D$^+$ is very helpful for searching massive starless cores (Kong et al. 2017). Furthermore, the SPW4 of the QUARKS survey is free of strong lines, and it is very useful for searching and studying COMs in hot cores (Figure 7), while recombination lines could help identify H II regions.

7. Summary

We have presented an overview of the ALMA-QUARKS survey. The survey is observing 139 protoclusters, consisting of 156 pointings with the ALMA at Band 6. These protoclusters were selected as the dense kernels of massive clumps revealed by the ATOMS survey. The primary goal of the QUARKS survey was to investigate the star formation process within protoclusters down to a scale of 1000 au in an unbiased and statistical manner. This paper has outlined the observations and data reduction of the QUARKS survey, and provides a first look at Sgr B2(M). The QUARKS surveys wide bandwidth (7.5 GHz) and high resolution ($\sim0\rlap{.}''3$) allow us to resolve more compact cores than the ATOMS survey, and detect previously unrevealed fainter filamentary structures. The spectral windows cover transitions of species such as CO, SO, N_2D^+, SiO, $H_{30}\alpha$, and many complex organic molecules, tracing gas components with varying temperatures and spatial extents. The unique observing setups of the QUARKS survey offer an opportunity to enhance our understanding of several scientific topics of star formation, including the mass transfer process inside protoclusters by hub-filamentary structures, the existence of massive starless cores, the physical and chemical properties of dense cores within protoclusters, and protocluster feedback. Preliminary analysis toward Sgr B2 (M2) indicates that our data reduction ensures high-quality continuum and spectral line data for realizing these scientific objectives. Specifically, the self-calibration approach can further improve data quality particularly for targeted sources with strong emission.

Acknowledgments

Appendix
Source Catalogue

Table A1 lists all the observed targets of the QUARKS survey, including the target names, coordinates, velocity (V_{LSR}), and distance (D). For velocity and distance, both of the values adopted by the ATOMS survey (marked by a superscript of "old") and the QUARKS survey (marked by a superscript of "new") are listed. Table A2 lists the continuum cores of Sgr B2(M) revealed by the QUARKS survey.

Table A1
The Targets of the QUARKS Survey[a]

ID	Target[b]	R.A. (J2000)	Decl. (J2000)	Glon (°)	Glat (°)	$V_{\mathrm{LSR}}^{\mathrm{old\ c}}$ (km s^{-1})	$V_{\mathrm{LSR}}^{\mathrm{new}}$ (km s^{-1})	D^{old} (kpc)	D^{new} (kpc)
1	I08303-4303	08:32:09.190	−43:13:44.30	261.645 03	−2.08742	14.3	14.5	2.3	2.35
2	I08448-4343_1	08:46:32.270	−43:54:35.70	263.771 91	−0.43510	3.7	2.8	0.7	1.22
3	I08448-4343_2	08:46:34.340	−43:54:30.50	263.774 67	−0.42935	3.7	2.8	0.7	1.22
4	I08470-4243	08:48:47.720	−42:54:22.00	263.248 57	+0.51455	12.0	12.1	2.1	2.27
5	I09002-4732	09:01:54.140	−47:44:09.30	268.421 88	−0.84936	3.1	3.2	1.2	1.62
6	I09018-4816	09:03:32.820	−48:28:06.20	269.152 12	−1.13009	10.3	9.9	2.6	2.57
7	I09094-4803	09:11:08.260	−48:15:54.60	269.852 80	−0.06249	74.6	74.4	9.6	8.75
8	I10365-5803_1	10:38:32.070	−58:19:01.10	286.206 19	+0.17153	−19.0	−20.1	2.4	2.49
9	I10365-5803_2	10:38:32.990	−58:19:16.70	286.210 07	+0.16873	−19.0	−20.1	2.4	2.5
10	I11298-6155	11:32:06.030	−62:12:20.50	293.827 78	−0.74454	32.9	33.4	10.0	9.6
11	I11332-6258	11:35:32.230	−63:14:46.80	294.511 78	−1.62216	−15.4	−15.4	1.9	1.4
12	I12320-6122	12:34:53.380	−61:39:46.90	300.969 16	+1.14564	−42.5	−43.2	3.43	4.17
13	I12326-6245	12:35:34.810	−63:02:32.10	301.135 83	−0.22582	−39.6	−39.5	4.61	4.21
14	I12383-6128	12:41:17.320	−61:44:38.60	301.730 81	+1.10402	−39.1	−39.4	3.27	4.12
15	I12572-6316_1	13:00:24.030	−63:32:31.90	303.930 08	−0.68782	30.9	30.4	11.57	11.63
16	I12572-6316_2	13:00:28.730	−63:32:37.30	303.938 75	−0.68962	30.9	30.4	11.57	11.63
17	I13079-6218_1	13:11:13.730	−62:34:40.20	305.208 34	+0.20641	−42.6	−41.3	3.8	3.11
18	I13079-6218_2	13:11:09.500	−62:34:39.70	305.200 26	+0.20717	−42.6	−41.3	3.8	3.11
19	I13080-6229	13:11:14.280	−62:44:58.30	305.196 21	+0.03514	−35.6	−35.7	3.8	2.68
20	I13111-6228	13:14:26.490	−62:44:28.30	305.562 39	+0.01301	−38.8	−39.5	3.8	2.97
21	I13134-6242	13:16:42.990	−62:58:29.30	305.798 86	−0.24386	−31.5	−32.0	3.8	4.93
22	I13140-6226	13:17:15.900	−62:42:27.00	305.887 61	+0.01594	−33.9	−34.4	3.8	4.88
23	I13291-6229_1	13:32:31.770	−62:45:11.80	307.615 19	−0.25577	−36.5	−37.6	2.9	2.66
24	I13291-6229_2	13:32:34.580	−62:45:27.00	307.619 81	−0.26079	−36.5	−37.6	2.9	2.66
25	I13291-6249	13:32:31.230	−63:05:21.80	307.560 83	−0.58746	−34.7	−33.4	7.61	7.72
26	I13295-6152	13:32:53.490	−62:07:49.30	307.755 82	+0.35251	−44.4	−44.7	3.89	3.27
27	I13471-6120	13:50:42.100	−61:35:14.90	309.920 84	+0.47748	−56.7	−57.8	5.46	5.17
28	I13484-6100	13:51:58.640	−61:15:43.30	310.144 16	+0.75912	−55.0	−55.3	5.4	6.64
29	I14013-6105	14:04:54.560	−61:20:10.70	311.625 68	+0.28912	−48.1	−55.4	4.12	3.9
30	I14050-6056	14:08:42.150	−61:10:43.00	312.107 77	+0.30909	−47.1	−47.6	3.42	3.19
31	I14164-6028	14:20:08.230	−60:42:05.00	313.575 82	+0.32418	−46.5	−46.7	3.19	2.95
32	I14206-6151	14:24:22.810	−62:05:22.70	313.575 83	−1.15400	−50.0	−49.7	3.29	3.19
33	I14212-6131_1	14:25:00.980	−61:44:57.50	313.765 82	−0.86186	−50.5	−50.8	3.44	3.29
34	I14212-6131_2	14:25:04.240	−61:44:46.40	313.772 92	−0.86125	−50.5	−50.8	3.44	3.29
35	I14382-6017	14:42:01.900	−60:30:22.50	316.139 01	−0.50189	−60.7	−60.7	7.69	7.75
36	I14498-5856	14:53:42.530	−59:08:53.20	318.049 37	+0.08691	−49.3	−50.2	3.16	2.99
37	I15122-5801	15:16:05.650	−58:11:39.60	321.052 51	−0.50580	−60.9	−60.9	9.26	8.73
38	I15254-5621	15:29:19.480	−56:31:23.20	323.459 06	−0.07914	−67.3	−68.6	4.0	4.42
39	I15290-5546	15:32:53.230	−55:56:09.60	324.200 74	+0.12008	−87.5	−88.3	6.76	7.94
40	I15384-5348	15:42:17.510	−53:58:28.20	326.448 10	+0.90660	−41.0	−41.1	1.82	2.41
41	I15394-5358	15:43:16.590	−54:07:14.70	326.474 65	+0.70271	−41.6	−40.5	1.82	2.38
42	I15411-5352	15:44:59.460	−54:02:14.30	326.724 94	+0.61576	−41.5	−41.8	1.82	2.41
43	I15437-5343	15:47:33.110	−53:52:43.90	327.119 42	+0.50904	−83.0	−83.4	4.98	5.16
44	I15439-5449	15:47:49.820	−54:58:28.10	326.473 10	−0.37656	−54.6	−54.8	3.29	3.4
45	I15502-5302	15:54:06.430	−53:11:38.40	328.307 50	+0.43085	−91.4	−92.4	5.8	5.49
46	I15520-5234	15:55:48.390	−52:43:09.80	328.807 64	+0.63243	−41.3	−41.8	2.65	2.56
47	I15522-5411_1	15:56:06.950	−54:19:58.90	327.807 53	−0.63475	−46.7	−47.5	2.73	2.89
48	I15522-5411_2	15:56:08.220	−54:19:35.70	327.814 03	−0.63179	−46.7	−47.5	2.73	2.89
49	I15557-5215	15:59:40.760	−52:23:27.70	329.469 07	+0.50244	−67.6	−68.5	4.03	6.91
50	I15567-5236	16:00:32.860	−52:44:45.10	329.337 43	+0.14749	−107.1	−107.5	5.99	5.22
51	I15570-5227	16:00:55.560	−52:36:25.20	329.471 66	+0.21497	−101.5	−100.7	5.99	5.64
52	I15584-5247	16:02:19.630	−52:55:28.40	329.422 99	−0.16370	−76.8	−76.4	4.41	4.87
53	I15596-5301	16:03:32.290	−53:09:28.10	329.405 76	−0.45907	−72.1	−73.7	10.11	9.2
54	I16026-5035_1	16:06:25.630	−50:43:18.10	331.359 20	+1.06314	−78.3	−79.0	4.53	5.05
55	I16026-5035_2	16:06:23.110	−50:43:26.10	331.352 77	+1.06593	−78.3	−79.0	4.53	5.05
56	I16037-5223	16:07:38.100	−52:31:00.20	330.294 33	−0.39406	−80.0	−81.3	9.84	9.04
57	I16060-5146	16:09:52.850	−51:54:54.70	330.954 19	−0.18248	−91.6	−92.1	5.3	5.39
58	I16065-5158	16:10:19.600	−52:06:07.10	330.877 88	−0.36624	−63.3	−62.5	3.98	4.33

Table A1
(Continued)

ID	Target[b]	R.A. (J2000)	Decl. (J2000)	Glon (°)	Glat (°)	$V_{\mathrm{LSR}}^{\mathrm{old\ c}}$ (km s^{-1})	$V_{\mathrm{LSR}}^{\mathrm{new}}$ (km s^{-1})	D^{old} (kpc)	D^{new} (kpc)
59	I16071-5142	16:10:59.010	−51:50:21.60	331.130 62	−0.24240	−87.0	−86.5	5.3	5.29
60	I16076-5134	16:11:27.120	−51:41:56.90	331.279 18	−0.18915	−87.7	−87.8	5.3	5.31
61	I16119-5048	16:15:45.650	−50:55:58.50	332.294 82	−0.09513	−48.2	−48.6	3.1	3.42
62	I16132-5039_1	16:17:01.920	−50:46:51.00	332.544 80	−0.12485	−47.5	−47.6	3.1	3.36
63	I16132-5039_2	16:17:02.690	−50:47:07.10	332.543 15	−0.12947	−47.5	−47.6	3.1	3.36
64	I16164-5046	16:20:10.910	−50:53:15.50	332.825 60	−0.54900	−57.3	−56.7	3.57	4.02
65	I16172-5028_1	16:21:02.930	−50:35:11.60	333.135 02	−0.43180	−51.9	−53.3	3.57	3.78
66	I16172-5028_2	16:21:00.160	−50:35:09.10	333.130 32	−0.42614	−51.9	−53.3	3.57	3.79
67	I16177-5018	16:21:31.490	−50:25:04.50	333.307 67	−0.36574	−50.2	−50.0	3.57	3.53
68	I16272-4837	16:30:58.020	−48:43:46.60	335.585 05	−0.28737	−46.6	−46.8	2.92	3.54
69	I16297-4757	16:33:29.290	−48:03:31.50	336.360 99	−0.13529	−79.6	−79.3	5.03	5.1
70	I16304-4710	16:34:04.800	−47:16:32.00	337.003 68	+0.32327	−62.8	−62.3	11.32	10.5
71	I16313-4729	16:34:55.440	−47:35:40.90	336.865 51	+0.00213	−73.7	−74.1	4.71	4.99
72	I16318-4724	16:35:33.200	−47:31:11.30	336.992 45	−0.02558	−119.8	−120.8	7.68	7.95
73	I16330-4725	16:36:42.600	−47:31:30.80	337.119 93	−0.17360	−75.1	−75.4	10.99	9.96
74	I16344-4658	16:38:10.380	−47:04:56.70	337.614 79	−0.06089	−49.5	−49.7	12.09	11.23
75	I16348-4654	16:38:29.420	−47:00:39.70	337.704 03	−0.05342	−46.5	−47.8	12.09	11.33
76	I16351-4722	16:38:50.610	−47:27:59.70	337.404 74	−0.40206	−41.4	−40.8	3.02	2.33
77	I16362-4639	16:39:57.700	−46:45:04.30	338.065 30	−0.06792	−38.8	−38.6	3.01	2.26
78	I16372-4545	16:40:54.770	−45:50:53.60	338.850 13	+0.40789	−57.3	−57.5	4.16	4.42
79	I16385-4619	16:42:13.980	−46:25:27.20	338.568 65	−0.14425	−117.0	−117.0	7.11	5.76
80	I16424-4531	16:46:06.610	−45:36:46.60	339.622 57	−0.12249	−34.2	−34.5	2.63	2.19
81	I16445-4459	16:48:05.180	−45:05:08.60	340.249 17	−0.04582	−121.3	−122.2	7.95	7.72
82	I16458-4512	16:49:30.410	−45:17:53.60	340.247 49	−0.37413	−50.4	−50.9	3.56	4.19
83	I16484-4603	16:52:03.990	−46:08:24.60	339.884 82	−1.25558	−32.0	−32.4	2.1	2.17
84	I16487-4423_1	16:52:23.670	−44:27:52.30	341.215 78	−0.23579	−43.4	−44.0	3.26	2.65
85	I16487-4423_2	16:52:21.590	−44:28:00.60	341.210 07	−0.23248	−43.4	−44.0	3.26	2.65
86	I16489-4431	16:52:34.080	−44:36:16.70	341.127 13	−0.34861	−41.3	−41.1	3.26	2.48
87	I16524-4300	16:56:03.060	−43:04:47.30	342.706 69	+0.12514	−40.8	−40.6	3.43	2.52
88	I16547-4247	16:58:17.260	−42:52:04.50	343.127 50	−0.06248	−30.4	−30.6	2.74	2.19
89	I16562-3959	16:59:41.450	−40:03:34.60	345.495 28	+1.47062	−12.6	−11.3	2.38	1.37
90	I16571-4029	17:00:32.380	−40:34:13.80	345.192 80	+1.02820	−15.0	−15.4	2.38	2.13
91	I17006-4215	17:04:13.200	−42:19:54.20	344.221 19	−0.59458	−23.2	−24.3	2.21	2.85
92	I17008-4040	17:04:23.200	−40:44:24.90	345.504 60	+0.34705	−17.0	−17.3	2.38	1.33
93	I17016-4124	17:05:11.020	−41:29:07.80	345.002 85	−0.22408	−27.1	−26.8	1.37	3.16
94	I17136-3617	17:17:02.290	−36:21:02.10	350.505 70	+0.95672	−10.6	−11.6	1.34	1.33
95	I17143-3700	17:17:45.650	−37:03:11.80	350.015 83	+0.43248	−31.1	−31.7	12.67	11.71
96	I17158-3901	17:19:20.340	−39:03:53.30	348.549 25	−0.97890	−15.2	−16.6	3.38	3.33
97	I17160-3707	17:19:27.310	−37:11:00.40	350.103 65	+0.08132	−69.5	−69.4	10.53	10.28
98	I17175-3544	17:20:53.570	−35:46:59.80	351.417 58	+0.64492	−5.7	−8.7	1.34	1.32
99	I17204-3636	17:23:50.320	−36:38:58.10	351.041 14	−0.33570	−18.2	−18.1	3.32	3.27
100	I17220-3609	17:25:24.990	−36:12:41.10	351.581 85	−0.35181	−93.7	−97.2	8.01	8.05
101	I17233-3606	17:26:42.800	−36:09:16.80	351.775 25	−0.53699	−2.7	−3.1	1.34	1.32
102	I17244-3536	17:27:48.710	−35:39:10.80	352.315 84	−0.44245	−10.2	−10.8	1.36	2.63
103	I17258-3637	17:29:17.130	−36:40:12.60	351.633 74	−1.25360	−11.9	−10.5	2.59	1.33
104	I17269-3312_1	17:30:15.200	−33:14:57.50	354.596 72	+0.46787	−21.0	−21.4	4.38	4.53
105	I17269-3312_2	17:30:14.120	−33:14:22.60	354.602 74	+0.47635	−21.0	−21.4	4.38	4.53
106	I17271-3439_1	17:30:26.210	−34:41:45.40	353.409 90	−0.36021	−18.2	−17.2	3.1	3.66
107	I17271-3439_2	17:30:27.710	−34:41:45.90	353.412 61	−0.36457	−18.2	−17.2	3.1	3.67
108	I17278-3541	17:31:14.070	−35:44:04.30	352.631 52	−1.06690	−0.4	−0.5	1.33	1.32
109	I17439-2845_1	17:47:09.060	−28:46:17.80	0.314 80	−0.20090	18.7	18.4	8.0	6.93
110	I17439-2845_2	17:47:07.190	−28:46:01.30	0.315 18	−0.19269	18.7	18.4	8.0	6.94
111	I17441-2822	17:47:19.790	−28:23:05.70	0.665 89	−0.03412	50.8	50.8	8.1	8.3
112	I17455-2800	17:48:41.630	−28:01:44.60	1.125 84	−0.10749	−15.6	−14.8	10.0	11.14
113	I17545-2357	17:57:34.490	−23:58:04.30	5.637 35	+0.23748	7.9	8.8	2.93	3.0
114	I17589-2312	18:01:58.000	−23:12:32.00	6.796 33	−0.25777	21.3	20.5	2.97	3.44
115	I17599-2148	18:03:01.470	−21:48:06.30	8.140 78	+0.22409	18.6	18.6	2.99	3.44

Table A1
(Continued)

ID	Target[b]	R.A. (J2000)	Decl. (J2000)	Glon (°)	Glat (°)	$V_{\mathrm{LSR}}^{\mathrm{old\ c}}$ (km s^{-1})	$V_{\mathrm{LSR}}^{\mathrm{new}}$ (km s^{-1})	D^{old} (kpc)	D^{new} (kpc)
116	I18032-2032	18:06:14.300	−20:31:35.00	9.619 69	+0.19657	4.3	4.4	5.15	4.8
117	I18056-1952	18:08:38.180	−19:51:49.00	10.472 49	+0.02752	66.7	66.4	8.55	8.44
118	I18075-2040	18:10:34.500	−20:39:16.10	10.000 23	−0.75297	31.5	31.2	3.08	2.8
119	I18079-1756	18:10:50.770	−17:55:45.20	12.418 44	+0.50544	18.0	17.8	1.83	2.32
120	I18089-1732	18:11:51.060	−17:31:27.20	12.888 63	+0.49074	33.5	32.9	2.5	3.64
121	I18110-1854	18:14:01.050	−18:53:23.30	11.937 13	−0.61570	37.0	38.5	3.37	3.17
122	I18116-1646	18:14:35.960	−16:45:36.80	13.873 86	+0.28067	48.5	48.8	3.94	3.86
123	I18117-1753	18:14:39.250	−17:51:59.80	12.908 11	−0.25932	36.7	37.1	2.57	3.63
124	I18134-1942	18:16:22.120	−19:41:27.00	11.497 42	−1.48527	10.6	10.5	1.25	1.25
125	I18139-1842	18:16:51.590	−18:41:34.70	12.430 83	−1.11328	39.8	39.8	3.02	3.0
126	I18159-1648	18:18:54.340	−16:47:45.90	14.332 25	−0.64324	22.0	22.4	1.48	2.83
127	I18182-1433	18:21:09.220	−14:31:46.80	16.585 84	−0.05082	59.1	59.3	4.71	3.66
128	I18223-1243	18:25:10.580	−12:42:22.20	18.654 73	−0.05887	44.8	45.0	3.37	3.46
129	I18228-1312	18:25:42.270	−13:10:17.00	18.303 43	−0.38990	32.3	32.8	3.21	3.2
130	I18236-1205	18:26:25.650	−12:03:57.60	19.363 48	−0.03031	25.9	26.1	2.17	2.88
131	I18264-1152	18:29:14.500	−11:50:19.50	19.884 76	−0.53396	43.2	43.6	3.33	3.35
132	I18290-0924_1	18:31:42.980	−09:22:26.00	22.350 97	+0.06876	84.2	84.0	5.34	4.69
133	I18290-0924_2	18:31:43.740	−09:22:19.00	22.354 13	+0.06689	84.2	84.0	5.34	4.69
134	I18308-0503_1	18:33:29.780	−05:01:04.30	26.419 61	+1.68770	42.9	42.6	3.1	3.75
135	I18308-0503_2	18:33:30.850	−05:00:58.70	26.423 03	+1.68447	42.9	42.6	3.1	3.75
136	I18311-0809	18:33:53.430	−08:07:14.40	23.710 65	+0.17082	113.0	112.9	6.06	6.27
137	I18314-0720_1	18:34:10.010	−07:18:00.30	24.470 44	+0.48830	101.5	101.3	5.82	6.15
138	I18314-0720_2	18:34:09.050	−07:17:50.80	24.470 95	+0.49303	101.5	101.3	5.82	6.15
139	I18316-0602	18:34:20.580	−05:59:41.60	25.649 15	+1.05073	42.8	42.7	2.09	3.76
140	I18317-0513	18:34:25.800	−05:10:53.50	26.381 34	+1.40596	42.1	41.8	2.18	3.73
141	I18317-0757	18:34:24.900	−07:54:47.60	23.954 60	+0.15119	80.7	81.2	4.79	4.7
142	I18341-0727	18:36:50.400	−07:24:48.00	24.674 87	−0.15227	112.7	113.1	6.04	6.39
143	I18411-0338	18:43:46.260	−03:35:23.90	28.863 43	+0.06630	102.8	103.5	7.41	5.46
144	I18434-0242	18:46:04.200	−02:39:18.30	29.957 23	−0.01729	97.2	97.5	5.16	4.76
145	I18440-0148	18:46:36.390	−01:45:22.00	30.818 28	+0.27376	97.5	97.6	5.16	6.04
146	I18445-0222	18:47:09.760	−02:18:47.60	30.385 96	−0.10410	86.9	86.6	5.16	6.24
147	I18461-0113	18:48:42.230	−01:10:05.40	31.580 61	+0.07556	96.1	96.0	5.16	5.67
148	I18469-0132	18:49:33.150	−01:29:06.20	31.395 33	−0.25773	87.0	86.6	5.16	4.91
149	I18479-0005	18:50:31.200	−00:01:56.00	32.798 60	+0.18954	14.6	14.6	12.96	12.87
150	I18507+0110	18:53:18.120	+01:15:00.10	34.256 91	+0.15530	57.2	58.2	1.56	3.23
151	I18507+0121	18:53:18.150	+01:25:22.40	34.410 81	+0.23402	57.9	57.8	1.56	3.09
152	I18517+0437	18:54:14.110	+04:41:43.10	37.430 00	+1.51849	43.9	43.9	2.36	2.36
153	I18530+0215	18:55:33.610	+02:19:09.00	35.465 73	+0.14083	74.1	76.9	4.67	5.08
154	I19078+0901	19:10:13.410	+09:06:10.40	43.165 81	+0.01086	2.9	6.2	11.11	11.49
155	I19095+0930	19:11:53.900	+09:35:45.90	43.794 14	−0.12749	43.7	43.8	6.02	9.07
156	I19097+0847	19:12:08.900	+08:52:07.80	43.178 04	−0.51881	58.0	58.2	8.47	7.83

Notes.
[a] This table contains 156 rows.
[b] The two pointing targets associated with the same source were denoted by suffixes "_1" and "_2".
[c] The V_{LSR} is the velocity revealed by surveys before the ATOMS survey. The $V_{\mathrm{LSR}}^{\mathrm{new}}$ is the velocity revealed by the H^{13}CO$^+$ data of the ATOMS survey. The D^{old} is the distance adopted by the ATOMS survey, originally derived from the Galactic rotation curve by Bronfman et al. (1996). The D^{new} is derived from the coordinate and $V_{\mathrm{LSR}}^{\mathrm{new}}$, using the distance calculator of Reid et al. (2016). See Section 2.1 for details.

Table A2
The Continuum Cores in Sgr B2(M) Detected by the QUARKS Survey[a]

Core ID	R.A. (J2000) (°)	Decl. (J2000) (°)	L_{max} ('')	L_{min} ('')	PA[b] (°)	I_{peak}[c] (Jy beam^{-1})	Flux[d] Jy	SM17[e]
1	266.834 03	−28.38466	0.9	0.7	−60.0	1.2384	2.9881(33)	Y
2	266.833 90	−28.38451	0.7	0.5	−48.0	1.0232	1.6362(19)	Y
3	266.833 77	−28.38439	0.5	0.5	0.0	0.4462	0.5199(7)	N
4	266.834 21	−28.38456	0.6	0.5	0.0	0.4320	0.4593(7)	N
5	266.833 79	−28.38418	0.6	0.5	0.0	0.2037	0.3029(5)	Y
6	266.833 93	−28.38489	0.7	0.6	0.0	0.3453	0.8302(11)	Y
7	266.834 09	−28.38502	0.6	0.5	0.0	0.3427	0.4357(5)	Y
8	266.833 62	−28.38459	0.8	0.6	−30.0	0.2454	0.3665(5)	N
9	266.833 83	−28.38510	0.6	0.6	−51.0	0.2598	0.4426(7)	Y
10	266.834 16	−28.38520	0.6	0.5	34.0	0.1956	0.3105(5)	Y
11	266.834 33	−28.38535	0.6	0.5	39.0	0.1103	0.1880(4)	Y
12	266.834 05	−28.38436	0.6	0.4	−6.0	0.3207	0.3038(5)	N
13	266.833 94	−28.38397	0.7	0.5	0.0	0.0739	0.1490(4)	Y
14	266.834 54	−28.38421	0.6	0.6	0.0	0.2274	0.2956(5)	Y
15	266.834 49	−28.38438	0.6	0.4	0.0	0.0627	0.0839(2)	Y
16	266.834 13	−28.38421	1.0	0.6	0.0	0.1171	0.3160(5)	N
17	266.833 79	−28.38378	1.0	0.5	41.0	0.0500	0.1045(4)	N
18	266.833 00	−28.38415	0.9	0.5	90.0	0.0638	0.1336(4)	Y
19	266.833 59	−28.38506	0.7	0.5	21.0	0.0984	0.2074(4)	Y
20	266.833 36	−28.38496	0.7	0.5	26.0	0.0696	0.1301(4)	N
21	266.833 14	−28.38486	0.7	0.5	15.0	0.0654	0.1284(4)	Y
22	266.832 92	−28.38476	0.8	0.5	23.0	0.0526	0.1140(4)	N
23	266.832 64	−28.38459	0.9	0.8	0.0	0.0295	0.0910(4)	N
24	266.832 37	−28.38441	0.8	0.7	0.0	0.0178	0.0388(2)	N
25	266.833 49	−28.38527	1.1	0.8	−65.0	0.0678	0.3022(7)	N
26	266.832 89	−28.38519	0.4	0.4	0.0	0.0213	0.0187(2)	N
27	266.833 80	−28.38579	0.9	0.6	−69.0	0.0520	0.1187(4)	Y
28	266.833 04	−28.38608	0.6	0.5	0.0	0.0360	0.0467(2)	Y
29	266.832 97	−28.38591	0.6	0.6	0.0	0.0239	0.0449(2)	N
30	266.833 06	−28.38560	0.7	0.6	0.0	0.0154	0.0369(2)	N
31	266.833 15	−28.38632	1.3	1.1	90.0	0.0190	0.1026(5)	N
32	266.833 40	−28.38643	0.6	0.5	−57.0	0.0118	0.0161(2)	N
33	266.832 72	−28.38625	0.7	0.5	0.0	0.0132	0.0193(2)	N
34	266.833 59	−28.38693	1.0	0.9	90.0	0.0171	0.0588(4)	N
35	266.833 78	−28.38710	0.7	0.6	40.0	0.0074	0.0160(2)	N
36	266.833 72	−28.38732	0.6	0.6	0.0	0.0055	0.0081(2)	N
37	266.834 35	−28.38749	0.7	0.5	0.0	0.0046	0.0013(2)	N
38	266.832 28	−28.38615	0.8	0.6	9.0	0.0234	0.0583(2)	N
39	266.832 07	−28.38595	0.6	0.5	38.0	0.0415	0.0597(2)	N
40	266.832 04	−28.38580	0.5	0.4	90.0	0.0262	0.0285(2)	Y
41	266.831 75	−28.38563	0.7	0.6	0.0	0.1086	0.1925(4)	Y
42	266.831 92	−28.38617	0.6	0.4	0.0	0.0207	0.0313(2)	N
43	266.831 93	−28.38633	0.6	0.5	0.0	0.0270	0.0367(2)	N
44	266.831 54	−28.38575	0.5	0.4	0.0	0.0245	0.0313(2)	N
45	266.831 51	−28.38605	0.8	0.7	90.0	0.0166	0.0451(2)	N
46	266.831 92	−28.38652	0.8	0.6	−8.0	0.0098	0.0205(2)	N
47	266.832 10	−28.38535	0.7	0.6	0.0	0.0284	0.0473(2)	Y
48	266.831 59	−28.38530	0.6	0.4	−39.0	0.0382	0.0480(2)	Y
49	266.831 66	−28.38539	0.4	0.3	0.0	0.0288	0.0217(2)	N
50	266.831 35	−28.38516	0.9	0.5	53.0	0.0124	0.0259(2)	N
51	266.831 11	−28.38526	0.6	0.4	0.0	0.0162	0.0165(2)	N
52	266.831 00	−28.38547	0.7	0.4	25.0	0.0474	0.0584(2)	Y
53	266.830 88	−28.38555	0.5	0.5	0.0	0.0251	0.0303(2)	N
54	266.830 62	−28.38583	0.9	0.6	0.0	0.0226	0.0458(2)	Y
55	266.831 09	−28.38703	0.6	0.6	0.0	0.0081	0.0059(2)	N
56	266.833 33	−28.38848	1.1	1.1	90.0	0.0100	0.0320(5)	N
57	266.831 48	−28.38423	0.6	0.5	0.0	0.0453	0.0664(2)	Y
58	266.831 51	−28.38408	0.4	0.4	90.0	0.0274	0.0228(2)	N

Table A2
(Continued)

Core ID	R.A. (J2000) (°)	Decl. (J2000) (°)	L_{max} (″)	L_{min} (″)	PA[b] (°)	I_{peak}[c] (Jy beam^{-1})	Flux[d] Jy	SM17[e]
59	266.831 18	−28.38441	0.5	0.5	0.0	0.0154	0.0154(2)	N
60	266.830 79	−28.38422	0.6	0.4	30.0	0.0231	0.0289(2)	Y
61	266.831 72	−28.38373	1.1	0.6	0.0	0.0063	0.0150(2)	N
62	266.831 21	−28.38339	0.5	0.5	0.0	0.0165	0.0174(2)	N
63	266.831 07	−28.38326	0.7	0.7	0.0	0.0221	0.0492(2)	Y
64	266.830 85	−28.38320	0.7	0.5	0.0	0.0137	0.0212(2)	N
65	266.830 39	−28.38351	1.6	1.1	−51.0	0.0067	0.0416(5)	N
66	266.830 07	−28.38412	0.5	0.4	0.0	0.0128	0.0106(2)	N
67	266.829 88	−28.38406	0.4	0.4	−55.0	0.0089	0.0079(2)	N
68	266.829 47	−28.38455	0.8	0.7	−31.0	0.0281	0.0585(2)	N
69	266.829 31	−28.38468	0.5	0.5	0.0	0.0082	0.0077(2)	N
70	266.829 23	−28.38447	0.7	0.6	0.0	0.0102	0.0193(2)	N
71	266.829 54	−28.38401	0.9	0.7	90.0	0.0096	0.0296(2)	N
72	266.829 39	−28.38363	0.5	0.4	0.0	0.0072	0.0063(2)	N
73	266.829 19	−28.38513	0.6	0.5	72.0	0.0087	0.0122(2)	N
74	266.829 01	−28.38517	0.5	0.4	0.0	0.0126	0.0114(2)	N
75	266.828 71	−28.38522	0.8	0.4	−25.0	0.0107	0.0172(2)	N
76	266.828 13	−28.38442	0.6	0.6	0.0	0.0399	0.0576(2)	N
77	266.828 37	−28.38439	0.5	0.5	0.0	0.0165	0.0187(2)	N
78	266.828 10	−28.38234	1.2	0.8	0.0	0.0306	0.1156(5)	N
79	266.833 54	−28.38364	0.8	0.5	0.0	0.0173	0.0367(2)	N
80	266.833 29	−28.38363	0.7	0.7	0.0	0.0099	0.0236(2)	N
81	266.833 33	−28.38305	1.1	0.9	0.0	0.0056	0.0184(4)	N
82	266.833 60	−28.38299	1.1	0.7	90.0	0.0055	0.0136(4)	N
83	266.833 82	−28.38290	0.8	0.7	0.0	0.0057	0.0132(2)	N
84	266.834 17	−28.38275	1.0	0.9	90.0	0.0074	0.0256(4)	N
85	266.831 35	−28.38218	1.1	0.9	90.0	0.0054	0.0133(4)	N
86	266.828 55	−28.38578	0.7	0.6	0.0	0.0115	0.0181(2)	N
87	266.834 17	−28.38583	0.9	0.8	90.0	0.0169	0.0597(4)	N
88	266.834 68	−28.38563	0.5	0.5	90.0	0.0233	0.0276(2)	N
89	266.834 69	−28.38546	0.6	0.5	15.0	0.0254	0.0431(2)	N
90	266.834 90	−28.38548	0.8	0.7	0.0	0.0219	0.0679(4)	Y
91	266.834 85	−28.38524	0.9	0.8	90.0	0.0239	0.0998(4)	N
92	266.834 96	−28.38479	1.5	1.0	−50.0	0.0580	0.3959(9)	Y
93	266.835 39	−28.38452	1.8	0.9	0.0	0.0358	0.2894(8)	N
94	266.835 04	−28.38655	1.9	1.8	0.0	0.0067	0.0579(8)	N
95	266.832 96	−28.38263	1.5	1.1	−56.0	0.0037	0.0067(5)	N
96	266.831 33	−28.38798	0.6	0.5	−30.0	0.0052	0.0062(2)	N
97	266.832 54	−28.38526	0.5	0.5	0.0	0.0043	0.0053(2)	N

Notes.
[a] This table contains 97 rows.
[b] The position angle (PA) is defined in the style of DS9. When PA is 0°, the major axis is in the direction of east. The major axis rotates from the east to the north when PA changes from 0° to 90°.
[c] The uncertainty of I_{peak} is estimated to be 1 mJy beam^{-1} for weak cores.
[d] The number in the bracket is the uncertainty of the last digital of the flux.
[e] Denote if the corresponding core has been identified by Sánchez-Monge et al. (2017).

ORCID iDs

Xunchuan Liu (刘训川) ● https://orcid.org/0000-0001-8315-4248
Xing Lu ● https://orcid.org/0000-0003-2619-9305
Anandmayee Tej ● https://orcid.org/0000-0001-5917-5751
Ken'ichi Tatematsu ● https://orcid.org/0000-0002-8149-8546

Qizhou Zhang ● https://orcid.org/0000-0003-2384-6589
Qilao Gu ● https://orcid.org/0000-0002-2826-1902
Anindya Saha ● https://orcid.org/0000-0002-9793-3039

References

Anderson, M., Peretto, N., Ragan, S. E., et al. 2021, MNRAS, 508, 2964
André, P., Men'shchikov, A., Bontemps, S., et al. 2010, A&A, 518, L102

Bally, J., Anderson, L. D., Battersby, C., et al. 2010, A&A, 518, L90
Bastian, N., Covey, K. R., & Meyer, M. R. 2010, ARA&A, 48, 339
Baug, T., Wang, K., Liu, T., et al. 2021, MNRAS, 507, 4316
Belloche, A., Menten, K. M., Comito, C., et al. 2008, A&A, 482, 179
Bonnell, I. A., & Bate, M. R. 2006, MNRAS, 370, 488
Bonnell, I. A., Vine, S. G., & Bate, M. R. 2004, MNRAS, 349, 735
Bronfman, L., Nyman, L. A., & May, J. 1996, A&AS, 115, 81
Budaiev, N., Ginsburg, A., Jeff, D., et al. 2023, Protostellar cores in Sagittarius
    B2 N and M, arXiv:2309.14407
Chen, H.-R. V., Keto, E., Zhang, Q., et al. 2016, ApJ, 823, 125
Cheng, Y., Tan, J. C., Liu, M., et al. 2018, ApJ, 853, 160
Chevance, M., Krumholz, M. R., McLeod, A. F., et al. 2023, in ASP Conf. Ser.
    534, Protostars and Planets VII, ed. S. Inutsuka et al. (San Francisco,
    CA: ASP), 1
Cyganowski, C. J., Brogan, C. L., Hunter, T. R., et al. 2014, ApJL, 796, L2
Faúndez, S., Bronfman, L., Garay, G., et al. 2004, A&A, 426, 97
Ge, Y., Wang, K., Duarte-Cabral, A., et al. 2023, A&A, 675, A119
Ginsburg, A., Bally, J., Barnes, A., et al. 2018, ApJ, 853, 171
Goldsmith, P. F., Lis, D. C., Hills, R., & Lasenby, J. 1990, ApJ, 350, 186
Gordon, M. A., & Sorochenko, R. L. 2002, Radio Recombination Lines. Their
    Physics and Astronomical Applications, Vol. 282 (Berlin: Springer)
Guesten, R., & Downes, D. 1983, A&A, 117, 343
Hacar, A., Clark, S. E., Heitsch, F., et al. 2023, in ASP Conf. Ser. 534,
    Protostars and Planets VII, ed. S. Inutsuka et al. (San Francisco, CA:
    ASP), 153
Heitsch, F., Hartmann, L. W., Slyz, A. D., Devriendt, J. E. G., & Burkert, A.
    2008, ApJ, 674, 316
Herrington, N. P., Dobbs, C. L., & Bending, T. J. R. 2023, MNRAS, 521, 5712
Johnston, K. G., Robitaille, T. P., Beuther, H., et al. 2015, ApJL, 813, L19
Kauffmann, J., Pillai, T., Zhang, Q., et al. 2017, A&A, 603, A89
Kong, S., Tan, J. C., Caselli, P., et al. 2017, ApJ, 834, 193
Könyves, V., André, P., Men'shchikov, A., et al. 2015, A&A, 584, A91
Krumholz, M. R., Bate, M. R., Arce, H. G., et al. 2014, in Protostars and
    Planets VI, ed. H. Beuther et al. (Tucson, AZ : Univ. Arizona Press), 243
Krumholz, M. R., Klein, R. I., & McKee, C. F. 2007, ApJ, 656, 959
Kumar, M. S. N., Arzoumanian, D., Men'shchikov, A., et al. 2022, A&A,
    658, A114
Kumar, M. S. N., Palmeirim, P., Arzoumanian, D., & Inutsuka, S. I. 2020,
    A&A, 642, A87
Lee, J.-E., Matsumoto, T., Kim, H.-J., et al. 2023, ApJ, 953, 82
Li, G.-X., Urquhart, J. S., Leurini, S., et al. 2016, A&A, 591, A5
Li, S., Sanhueza, P., Zhang, Q., et al. 2020, ApJ, 903, 119
Liu, H.-L., Liu, T., Evans, N. J. I., et al. 2021a, MNRAS, 505, 2801
Liu, H.-L., Tej, A., Liu, T., et al. 2022a, MNRAS, 511, 4480
Liu, H.-L., Tej, A., Liu, T., et al. 2022b, MNRAS, 510, 5009
Liu, H.-L., Tej, A., Liu, T., et al. 2023a, MNRAS, 522, 3719
Liu, R., Liu, T., Chen, G., et al. 2022c, MNRAS, 511, 3618
Liu, T., Evans, N. J., Kim, K.-T., et al. 2020a, MNRAS, 496, 2790
Liu, T., Evans, N. J., Kim, K.-T., et al. 2020b, MNRAS, 496, 2821
Liu, T., Kim, K.-T., Juvela, M., et al. 2018, ApJS, 234, 28
Liu, T., Kim, K.-T., Yoo, H., et al. 2016, ApJ, 829, 59
Liu, X., Liu, T., Shen, Z., et al. 2022d, ApJS, 263, 13
Liu, X., Liu, T., Shen, Z., et al. 2023b, A&A, 671, L1
Liu, X. C., Wu, Y., Zhang, C., et al. 2021b, ApJ, 912, 148
Lu, X., Cheng, Y., Ginsburg, A., et al. 2020, ApJL, 894, L14
McGuire, B. A. 2022, ApJS, 259, 30

McKee, C. F., & Tan, J. C. 2003, ApJ, 585, 850
McMullin, J. P., Waters, B., Schiebel, D., Young, W., & Golap, K. 2007, in
    ASP Conf. Ser. 376, Astronomical Data Analysis Software and Systems
    XVI, ed. R. A. Shaw, F. Hill, & D. J. Bell (San Francisco, CA: ASP), 127
Meng, F., Sánchez-Monge, Á., Schilke, P., et al. 2019, A&A, 630, A73
Meng, F., Sánchez-Monge, Á., Schilke, P., et al. 2022, A&A, 666, A31
Möller, T., Schilke, P., Sánchez-Monge, Á., Schmiedeke, A., & Meng, F.
    2023, A&A, 676, A121
Morii, K., Sanhueza, P., Nakamura, F., et al. 2023, ApJ, 950, 148
Moscadelli, L., Rivilla, V. M., Cesaroni, R., et al. 2018, A&A, 616, A66
Motte, F., Bontemps, S., Csengeri, T., et al. 2022, A&A, 662, A8
Müller, H. S. P., Thorwirth, S., Roth, D. A., & Winnewisser, G. 2001, A&A,
    370, L49
Myers, A. T., McKee, C. F., Cunningham, A. J., Klein, R. I., &
    Krumholz, M. R. 2013, ApJ, 766, 97
Offner, S. S. R., Hansen, C. E., & Krumholz, M. R. 2009, ApJL, 704, L124
Olguin, F. A., Sanhueza, P., Ginsburg, A., et al. 2022, ApJ, 929, 68
Ossenkopf, V., & Henning, T. 1994, A&A, 291, 943
Padoan, P., Pan, L., Juvela, M., Haugbølle, T., & Nordlund, Å. 2020, ApJ,
    900, 82
Peng, Y., Liu, T., Qin, S.-L., et al. 2022, MNRAS, 512, 4419
Peretto, N., Fuller, G. A., Duarte-Cabral, A., et al. 2013, A&A, 555, A112
Peters, T., Naab, T., Walch, S., et al. 2017, MNRAS, 466, 3293
Pineda, J. E., Arzoumanian, D., Andre, P., et al. 2023, in ASP Conf. Ser. 534,
    Protostars and Planets VII, ed. S. Inutsuka et al. (San Francisco, CA:
    ASP), 233
Pineda, J. E., Segura-Cox, D., Caselli, P., et al. 2020, NatAs, 4, 1158
Pouteau, Y., Motte, F., Nony, T., et al. 2022, A&A, 664, A26
Pouteau, Y., Motte, F., Nony, T., et al. 2023, A&A, 674, A76
Qin, S.-L., Liu, T., Liu, X., et al. 2022, MNRAS, 511, 3463
Reid, M. J., Dame, T. M., Menten, K. M., & Brunthaler, A. 2016, ApJ, 823, 77
Reid, M. J., Menten, K. M., Brunthaler, A., et al. 2014, ApJ, 783, 130
Richards, A. M. S., Moravec, E., Etoka, S., et al. 2022, arXiv:2207.05591
Sanhueza, P., Contreras, Y., Wu, B., et al. 2019, ApJ, 886, 102
Sanhueza, P., Girart, J. M., Padovani, M., et al. 2021, ApJL, 915, L10
Sanna, A., Kölligan, A., Moscadelli, L., et al. 2019, A&A, 623, A77
Sánchez-Monge, Á., Schilke, P., Schmiedeke, A., et al. 2017, A&A, 604, A6
Schisano, E., Molinari, S., Elia, D., et al. 2020, MNRAS, 492, 5420
Schneider, N., Simon, R., Guevara, C., et al. 2020, PASP, 132, 104301
Schuller, F., Menten, K. M., Contreras, Y., et al. 2009, A&A, 504, 415
Taniguchi, K., Sanhueza, P., Olguin, F. A., et al. 2023, ApJ, 950, 57
Vázquez-Semadeni, E., Gómez, G. C., Jappsen, A. K.,
    Ballesteros-Paredes, J., & Klessen, R. S. 2009, ApJ, 707, 1023
Wang, K., Zhang, Q., Testi, L., et al. 2014, MNRAS, 439, 3275
Wang, K., Zhang, Q., Wu, Y., Li, H.-b., & Zhang, H. 2012, ApJL, 745, L30
Wyrowski, F., Schilke, P., Walmsley, C. M., & Menten, K. M. 1999, ApJL,
    514, L43
Xu, F., Wang, K., Liu, T., et al. 2023a, arXiv:2309.14684
Xu, F.-W., Wang, K., Liu, T., et al. 2023b, MNRAS, 520, 3259
Yang, D., Liu, H.-L., Tej, A., et al. 2023, ApJ, 953, 40
Yuan, J., Li, J.-Z., Wu, Y., et al. 2018, ApJ, 852, 12
Zhang, C., Evans, N. J., Liu, T., et al. 2022, MNRAS, 510, 4998
Zhang, C., Zhu, F.-Y., Liu, T., et al. 2023a, MNRAS, 520, 3245
Zhang, S., Wang, K., Liu, T., et al. 2023b, MNRAS, 520, 322
Zhou, J.-W., Liu, T., Evans, N. J., et al. 2022, MNRAS, 514, 6038
Zinnecker, H., & Yorke, H. W. 2007, ARA&A, 45, 481